

Genomic and epigenomic adaptation in SP-R210 (Myo18A) isoform-deficient macrophages

1 Eric Yau^{1,^,*}, Yan Chen^{1,2,^}, Chunhua Song^{3,4}, Jason Webb¹, Marykate Carillo¹, Yuka Imamura
2 Ikawasawa⁵, Zhenyuan Tang², Yoshinori Takahashi², Todd M Umstead¹, Sinisa Dovat², Zissis C.
3 Chroneos^{1,*}

4 ¹Department of Pediatrics and Microbiology and Immunology, Pulmonary Immunology and
5 Physiology Laboratory, Pennsylvania State University College of Medicine, Pennsylvania, USA

6 ²Department of Pediatrics, Union Hospital, Tongji Medical College, Huazhong University of Science
7 and Technology, Wuhan, China

8 ³Department of Pediatrics, Division of Pediatric Hematology and Oncology, Pennsylvania State
9 University College of Medicine, Pennsylvania, USA

10 ⁴Department of Internal Medicine, Ohio State University College of Medicine, Columbus, Ohio, USA

11 ⁵Department of Pharmacology and Biochemistry and Molecular Biology, Institute for Personalized
12 Medicine, Pennsylvania State University College of Medicine, Pennsylvania, USA

13

14 *Correspondence:

15 Eric Yau: eyau@pennstatehealth.psu.edu, and

16 Zissis C. Chroneos: zchroneos@pennstatehealth.psu.edu

17 ^Authors with equal contribution

18

19 **Keywords:** Macrophage Phenotype and function, PU.1 SP-R210 (Myo18A) isoforms, Influenza, Anti-
20 viral inflammation.

21

22 **1 Abstract**

23 Macrophages play fundamental roles in regulation of inflammatory responses to pathogens,
24 resolution of inflammation and tissue repair, and maintenance of tissue homeostasis. The long (L)
25 and short (S) isoforms of SP-R210/MYO18A, a macrophage receptor for surfactant protein A (SP-A)
26 and C1q, regulate basal and inflammatory macrophage phenotype at multiple gene expression,
27 translational, and subcellular levels in addition to their SP-A and C1q-mediated functions; disruption
28 of L renders macrophages hyper-inflammatory, although the underlying mechanism had previously
29 been unexplored. We asked whether disruption of the L isoform led to the hyper-inflammatory
30 state via alteration of global genomic responses. RNA sequencing analysis of SP-R210_L(DN)
31 macrophages revealed basal and influenza induced upregulation of genes associated with
32 inflammatory pathways, including TLR, RIG-I, NOD, and cytoplasmic DNA signaling, whereas
33 knockdown of both SP-R210 isoforms (L and S) only resulted in increased RIG-I and NOD signaling.
34 Chromatin immunoprecipitation sequencing (ChIP-seq) analysis showed increased genome-wide
35 deposition of the pioneer transcription factor PU.1 in SP-R210_L(DN) compared to WT cells. ChIP-seq
36 analysis of histone H3 methylation showed alterations in both repressive (H3K9me3 and H3K27me3)
37 and transcriptionally active (H3K9me3) histone marks. Influenza A virus (IAV) infection, which
38 stimulates an array of cytosolic and TLR-mediated antiviral mechanisms, resulted in differential
39 redistribution between proximal promoter and distal sites and decoupling of PU.1 binding from Toll-
40 like receptor regulated gene promoters in SP-R210_L(DN) cells. Our findings suggest that SP-R210_L-
41 deficient macrophages are poised with an open PU.1-primed chromatin conformation to rapidly
42 respond to inflammatory and metabolic stimuli.

43

44 2 Introduction

45 Macrophage functions are dynamic, alternating between pro-inflammatory responses to
46 pathogens and stress, and anti-inflammatory responses to alleviate injury to facilitate tissue repair
47 (Sica and Mantovani, 2012, Italiani and Boraschi, 2014, Stout, et al., 2005). Controlling this plasticity
48 is particularly important in the context of alveolar macrophages, the resident immune cell of the
49 lungs (Hussell and Bell, 2014, McQuattie-Pimentel, et al., 2021). As our lungs are exposed to
50 pollutants, pathogens, and particulates on a daily basis that can result in injury, infection, and
51 damage, this fluidity to regulate inflammatory activation state is particularly important for alveolar
52 macrophages to maintain lung homeostasis and avoid overt inflammation (Upham, et al., 1995,
53 Kobzik, et al., 1990). GM-CSF, the transcription factors PU.1 and PPAR γ , and the local
54 microenvironment consisting of surfactant proteins and lipids drive alveolar macrophage (AM)
55 development, differentiation, and function (McQuattie-Pimentel, et al., 2021, Shibata, et al., 2001,
56 Baker, et al., 2010, Chroneos, et al., 2010, Guilliams, et al., 2013, Bates, et al., 1997, Schneider, et al.,
57 2014).

58 Unlike circulating monocyte-derived macrophages, alveolar macrophages are derived from
59 monocyte progenitors in the yolk sac and fetal liver, which then migrate to the lung during fetal
60 development (Guilliams, et al., 2013, Tan and Krasnow, 2016). Early studies depleting alveolar
61 macrophages in mice showed that they play a critical role in pathogen clearance, similar to
62 circulating monocyte-derived macrophages. AMs secrete anti-microbial cytokines such as type I
63 IFNs, phagocytose pathogens, and act as antigen presenting cells to bridge the innate and adaptive
64 immune systems (He, et al., 2017, Kirby, et al., 2009). Depletion of alveolar macrophages also
65 results in overt inflammatory responses in mice exposed to sensitizing proteins, in particular
66 through secretion of cytokines like TGF β , IL-10, and prostaglandins (Roth and Golub, 1993). Alveolar
67 macrophages are critical for host survival and resolution of influenza infection (Schneider, et al.,
68 2014, Purnama, et al., 2014, Halstead, et al., 2018, Halstead and Chroneos, 2015). AMs are thus
69 critical in maintaining the anti-inflammatory state of the lung under normal conditions, and to
70 resolve inflammation that occurs during pulmonary infections caused not only by the pathogen
71 itself, but also by the host inflammatory response.

72 The unique microenvironment of the lung alveolus consists of surfactant proteins that work
73 in concert with alveolar macrophages to regulate immune balance, host defense, and tissue

74 homeostasis (Chroneos, et al., 2010, Casals, et al., 2019, Minutti, et al., 2017). Surfactant proteins
75 are part of the lipoprotein surfactant complex that reduces alveolar surface tension to maintain
76 alveolar gas-exchange, alveolar stability, and alveolar recruitment during breathing (Canadas, et al.,
77 2020, Autilio and Perez-Gil, 2019). There are two hydrophobic (SP-B, SP-C) and two hydrophilic lipid-
78 binding (SP-A, SP-D) surfactant proteins, all having amino-terminal domains that are important for
79 oligomerization into lipid-dependent and lipid-independent supramolecular structures. SP-B and SP-
80 C are critical for the formation of the surface tension lowering surfactant monolayer at the air-liquid
81 interface, whereas SP-A and SP-D modulate ultrastructural organization of the surfactant
82 phospholipid sub-phase. Within this milieu, the surfactant proteins enhance pathogen clearance
83 and coordinate immune and metabolic functions of alveolar macrophages, alveolar epithelial cells,
84 and their cross-talk with innate and adaptive immune cells. Under basal conditions, SP-A maintains
85 alveolar macrophages at an anti-inflammatory state by a number of mechanisms that include
86 increasing expression of the transcription factor IRAK-M (Nguyen, et al., 2012), global effects on
87 macrophage proteome composition enriched in anti-inflammatory pathways (Phelps, et al., 2013,
88 Phelps, et al., 2011), scavenging of pro-inflammatory mediators (Minutti, et al., 2016, Francisco, et
89 al., 2020), suppression of NF κ B activation (Younis, et al., 2020, Moulakakis, et al., 2016, Moulakakis
90 and Stamme, 2009, Wu, et al., 2004), and modulating trafficking of innate receptors (Henning, et al.,
91 2008, Gil, et al., 2009).

92 SP-A modulates the optimal relative expression of the long and short isoforms of the SP-A
93 receptor, SP-R210_L and SP-R210_S, on alveolar macrophages (Nguyen, et al., 2012, Yang, et al., 2015).
94 SP-R210 tailors SP-A-mediated phagocytosis of SP-A opsonized pathogens and pathogen-dependent
95 inflammatory responses by macrophages (Weikert, et al., 2000, Weikert, et al., 1997, Minutti, et al.,
96 2017). These isoforms are encoded by alternatively spliced mRNAs of the *Myo18A* gene (Mori, et al.,
97 2003, Yang, et al., 2005, Szeliga, et al., 2005), which generate tissue and cell-type specific isoforms
98 on the cell surface and subcellular organelles (Mori, et al., 2003, Yang, et al., 2005, Szeliga, et al.,
99 2005, Taft and Latham, 2020, Lee, et al., 2014, Ng, et al., 2013, Horsthemke, et al., 2019, Cross, et
100 al., 2004). MYO18A isoforms have so far been classified into three broad groups, MYO18A α ,
101 MYO18A β , and MYO18A γ , which are functionally diverse, catalytically inactive members of the
102 myosin superfamily. SP-R210_L (aka CD245 α) and SP-R210_S (aka CD245 β) are members of the
103 MYO18A α and MYO18A β groups on the surface of macrophages and other immune cells (Yang, et
104 al., 2005, De Masson, et al., 2016, Samten, et al., 2008), respectively. SP-R2120_L is induced during

105 terminal macrophage differentiation (Mori, et al., 2003). SP-R210/MYO18A isoforms are
106 differentially expressed with different relative abundance in myelomonocytic lineage cells (Mori, et
107 al., 2003, Cross, et al., 2004, Samten, et al., 2008, Chroneos and Shepherd, 1995), although the role
108 of each isoform and impact of SP-R210 isoform stoichiometry in macrophage development and
109 function is not understood at the molecular, cellular levels, and organismal levels. Bone marrow-
110 derived macrophages, monocytes, and immature myelomonocytic cells only express SP-R210_s,
111 whereas peritoneal and alveolar macrophages express both isoforms (Yang, et al., 2005, Cross, et al.,
112 2004, Samten, et al., 2008). Previous studies demonstrated that SP-R210 regulates extrinsic ligand-
113 dependent and intrinsic ligand-independent macrophage functions (Yang, et al., 2015, Weikert, et
114 al., 2000, Weikert, et al., 1997, Minutti, et al., 2017, Mori, et al., 2003, Yang, et al., 2005, Cross, et al.,
115 2004, Samten, et al., 2008, Jean Beltran, et al., 2016, Sever-Chroneos, et al., 2011, Borron, et al.,
116 1998, Chroneos, et al., 1996, Lopez-Sanchez, et al., 2010). Ligand-dependent functions include SP-A-
117 mediated bacterial phagocytosis coupled to production of reactive nitrogen species, secretion of
118 TNF α and increased macrophage responsiveness to IFN γ and IL-4. These functions facilitate killing
119 and eradication of bacterial and parasitic pathogens by alveolar macrophages (Weikert, et al., 2000,
120 Weikert, et al., 1997, Minutti, et al., 2017, Sever-Chroneos, et al., 2011, Stamme, et al., 2000). In the
121 context of an immune memory response, however, the interaction of SP-A with SP-R210 may limit
122 excessive activation of immune system-mediated inflammation (Samten, et al., 2008, Borron, et al.,
123 1998). SP-R210 may exacerbate injurious inflammation by peritoneal macrophages in the presence
124 of other ligands such as C1q (Minutti, et al., 2017), which is more abundant systemically, and innate
125 immune cell cytotoxicity by SP-A or other ligands in different tissues (De Masson, et al., 2016).
126 Studies in SP-R210_L-deficient macrophages revealed that depletion of the L isoform resulted in
127 broad baseline alterations in expression, trafficking and cell-surface localization of innate receptors,
128 and hyper-responsiveness to inflammatory stimuli (Yang, et al., 2015), suggesting global effects on
129 macrophage phenotype and function. However, the role that SP-R210 isoforms play in macrophage
130 function are not well-defined. Therefore, we asked whether differences in SP-R210 isoform
131 expression patterns shape the basal macrophage phenotype and responses to infection at genomic,
132 transcriptomic, and epigenomic levels. We found that alteration of SP-R210 isoform expression
133 resulted in distinct gene expression patterns that reflected changes in epigenetic remodeling and
134 chromatin accessibility in SP-R210_L-depleted macrophages. Additionally, using influenza as a model

135 of infection, our findings support the notion that SP-R210 isoforms coordinate nuclear responses to
136 infection in macrophages.

137

138 **3 Materials and Methods**

139 **3.1 Cell lines and Cell Culture**

140 SP-R210_L-deficient RAW 264.7 macrophages (SP-R210_L(DN)) were generated and characterized as
141 described previously by stable transfection of a pTriex-2 vector expressing the carboxy-terminal
142 domain of SP-R210 (SP-R210_L(DN)) cells (Yang, et al., 2015, Yang, et al., 2005, Sever-Chroneos, et al.,
143 2011). Most experiments utilized the SP-R210_L(DN) clone DN2 (Yang, et al., 2015, Yang, et al., 2005,
144 Sever-Chroneos, et al., 2011) unless otherwise noted in Figure legend. Control cells were
145 transfected with empty vector. The deletion of both SP-R210 isoforms was achieved using
146 CRISPR/Cas9. Guide RNA sequences targeting exons 5, 6, 12, and 14 were designed using
147 crispr.mit.edu and gRNA oligonucleotides were ligated into the LRG hU6-sgRNA- EFS-GFP-P2A
148 vector. RAW 264.7 macrophages were transduced with a Cas9 containing lentivirus and selected
149 using blasticidin to generate a stable Cas9 expressing cell line. Stable Cas9 RAW264.7 cells were
150 transfected with a pooled library of ligated gRNA vectors. Transfected GFP+ cells were isolated by
151 flow activated cell sorting into 96-well plates to culture individual clones. SP-R210-deficient clones
152 lacking both isoforms, designated, SP-R210(KO), were identified by Western blot analysis following
153 sorting (Supplemental Figure 1), and a single clone retaining deletion of both isoforms after
154 subculture was selected for further studies. Cells were maintained in DMEM culture media (DMEM
155 with 4.5 g/L glucose, L-glutamine, and sodium pyruvate supplemented with 10% heat-inactivated
156 fetal bovine serum (FBS) and 1% penicillin/streptomycin) at 37°C and 5% CO₂ in 10-cm dishes. Cells
157 were sub-cultured in 10-cm dishes x 5 at a density of 1 x 10⁷ cells/dish for ChIP-seq experiments,
158 sub-cultured in 6-well plates at a density of 1 x 10⁶ cells/well for RNA isolations (subjected to RNA-
159 seq experiments), or 24-well plates at 2 x 10⁵ cells/well for flow cytometry and other assays.

160 **3.2 Virus Preparation**

161 The mouse adapted influenza virus strain A/Puerto Rico/8/34 (PR8) influenza was propagated in the
162 allantoic fluid of embryonated chicken eggs (Sever-Chroneos, et al., 2011). Briefly, 10⁵ fluorescent

163 focus units (FFC) in PBS with 1% Penicillin/Streptomycin/Fungizone was injected into the amniotic
164 sac of 10 day old embryonated chicken eggs. Infected eggs were incubated at 37°C for 56 hours.
165 Eggs were then removed and placed at 4°C for 12 hours. The allantoic fluid was collected and spun
166 down at 131,000g for 40 minutes at 4°C. The virus pellet was reconstituted in PBS and layered over
167 a 30%/35%/50%/60% sucrose gradient and spun at 168,000g for 1 hour and 15 minutes and the
168 virus containing layer between 50% and 35% was collected and dialyzed against PBS at 4°C
169 overnight. The viral titer was determined by fluorescent plaque assays using Madine-Darby Canine
170 Kidney (MDCK) epithelial cells (ATCC Cat #CRL-2936) were plated in 96 well plates at a density of
171 3×10^4 serial dilutions of purified and dialyzed virus was overlaid on the cells. Cells were incubated
172 at 37°C with virus for 2 hours, at which point virus-containing media was replaced with virus-free
173 media and cells were incubated for another 6 hours. Cells were then fixed with acetone, and stained
174 with an Influenza A NP antibody (Sigma Aldrich Cat#MAB8251, 1:100 in PBS) for 30 minutes at 4°C
175 and subsequently labeled with Rhodamine conjugated anti-mouse IgG (Jackson ImmunoResearch,
176 Cat#115-026-062, 1:100 in PBS). Fluorescently labeled nuclei were counted using a Nikon Eclipse
177 TE2000-U at 20x magnification.

178 **3.3 Influenza Infection and Assessment of Infection**

179 Cells plated for infection were seeded at a density of 1×10^7 (ChIP-seq) or 2×10^5 per well for 12 hours
180 prior to infection. Cells were washed with PBS twice and PR8 virus was added at MOI 1 (ChIP-seq) or
181 MOI 4 (cytokine elaboration studies, influenza infection studies) in infection media (1:1 ratio DMEM
182 w/o serum to PBS) as determined by cell seeding density. Cells with infection media were incubated
183 at 37°C for two hours. Infection media were removed and replaced with DMEM culture media.
184 Infection was allowed to progress for another 10 hours or until the desired incubation time was
185 reached. Influenza infection was assessed via viral protein production by western blot (methods
186 outlined in 2.4), viral NP qPCR, and viral NP imaging. Supernatant and cell pellets from infected
187 samples were collected 12 hours post infection. qPCR was performed in accordance to Fino et al
188 (Fino, et al., 2017). RNA was prepared using the RNA-bee (Tel-Test, Inc. Cat #CS-501B) protocol for
189 cell supernatant and cell pellet. cDNA was synthesized with the High Capacity cDNA Reverse
190 Transcription Kit (Invitrogen Cat#4368814) using the IAV MP primer 5' TCT AAC CGA GGT CGA AAC
191 GTA 3' for IAV following the manufacturer's protocol. The cDNA was diluted five-fold prior and PCR
192 amplified using the TaqMan Fast Universal PCR Master Mix (ThermoFisher Cat#4305719). The PR8

193 M1 gene was amplified using the following primers: sense: 5'-AAG ACC AAT CCT GTC ACC TCTG A-3'
194 and antisense: 5'-CAA AGC GTC TAC GCT GCA GTC -3', 900nM each and the 200nM probe
195 sequence: 5'-/56-FAM/ TTT GTG TTC ACG CTC ACC GT/36-TAMSp/-3'. Immunofluorescence of IAV-
196 infected cells was performed on PR8 infected cells PR8 at MOI10 after 15 and 30 minutes. Infected
197 cells were fixed using 3.7% formaldehyde for 25 minutes. Fixed cells were blocked with 10% donkey
198 serum and 3% BSA in 0.2% Tween 20 in PBS. Blocked cells were probed using Rab5 (Cell Signaling
199 Technology Cat#3547S, 1:200) and NP (BioRad Cat#MCA400, 1:1000) overnight at 4°C, and labeled
200 using AF488 conjugated anti-mouse IgG (Jackson ImmunoResearch Cat#715-545-150, 1:500) and
201 AF594 conjugated anti-rabbit IgG (Jackson ImmunoResearch Cat#711-585-152, 1:500) for 2 hours at
202 room temperature. Cells were acquired using Nikon Eclipse Ti confocal microscope and Nikon
203 Elements 4.30.01 software.

204 **3.4 Western blot analysis**

205 Samples were harvested using 0.25% Trypsin-EDTA (Corning Cat#25-053-CI); lifted cells were
206 centrifuged at 15,000g for 5 minutes at 4°C (Eppendorf 5430R). Cell pellets were placed at -20°C
207 overnight with 60 µL SDS Lysis buffer (1% SDS, 50mM Tris-HCL pH 8.1, 10mM EDTA pH 8.0) with 1x
208 Protease/Phosphatase Inhibitor Cocktail (Cell Signaling Cat#5872S). Samples were thawed and
209 sonicated at 50% A for 10 seconds in 2 second ON/OFF intervals. Sonicated samples were
210 centrifuged at 15,000g for 5 minutes at 22°C. Supernatant was collected; 4x LDS sample buffer
211 (Invitrogen Cat#NP007) was added to a final concentration of 1x.

212 For gel electrophoresis, samples were diluted to 1X SDS-PAGE sample buffer, boiled at 90°C for 2
213 minutes, and centrifuged for 2 minutes at 21,000g. Equal volumes of protein were via in 4-12% Bis-
214 Tris gels (Invitrogen, Cat#NP0321BOX, NP0349BOX) for reducing gels and 4-12% Bis0Tris
215 NativePAGE gels (Invitrogen, Cat #BN1002BOX) for native, nonreducing gels and transferred using
216 eBlot L1 Transfer system (GenScript). Blots were blocked in 5% Bovine Serum Albumin (BSA) in 0.1%
217 Tween 20 in Tris-buffered saline (0.1% TBST). Blots were probed at 4°C overnight with MYO18A
218 (Proteintech Cat#14611-1-AP, 1:1000), p-IRF3 Ser396 (Cell Signaling Technology Cat#29047, 1:1000),
219 IRF3 (Cell Signaling Technology Cat#4302, 1:1000), p-IRF7 Ser437 (Cell Signaling Technology
220 Cat#24129, 1:1000), IRF7 (Aviva Systems Biology Cat#OAAN00009), p-p65 Ser276 (Thermo Fisher
221 Cat#PA5-37718, 1:1000), p-p65 Ser536 (Cell Signaling Technology Cat#3033, 1:1000), NFκB p65 (Cell
222 Signaling Technology Cat#8242, 1:1000), STING (Cell Signaling Technology Cat#50494, 1:1000), or

223 GAPDH (Thermo Fisher Cat#PA1-16777, 1:5000) in 0.1% BSA in 0.1% TBST and subsequently imaged
224 using HRP-conjugated anti-rabbit antibodies (Bio-Rad Cat#172-1019, 1:10000) and Western
225 Lightning Plus-ECL (PerkinElmer Cat#E1103001EA) on a BioRad Chemidoc imager. Images were
226 adjusted and band densitometry was determined using ImageLab 5.2.1. PU.1 (Invitrogen Cat #MA5-
227 15064, 1:500-1000), NS1 (Invitrogen Cat #PIPA532243, 1:1000), NP (BioRad Cat#MCA400, 1:1000),
228 and anti- β -actin (Sigma Aldrich Cat #A2228-100UL, 1:20000) blots were incubated with the relevant
229 primary antibodies at 4°C overnight and imaged using with IRDye 680RD anti-Mouse IgG (LI-COR
230 Cat#926-68070, 1:15000) and IRDye 800 CW anti-Rabbit IgG (LI-COR Cat#926-32211, 1:10000). Blots
231 were imaged using LI-COR Odyssey CLx and Image Studio 4.0. Band densitometry was acquired and
232 images were adjusted using Image Studio Lite 5.2.5.

233 **3.5 Cytokine analysis**

234 Cytokines were assessed from clarified supernatant using R&D Quantikine ELISA kits for TNF α (R&D
235 Systems, Cat#MTA00B) and DuoSet ELISA kits for IFN β (R&D Systems, Cat#DY8234-05). 500 μ L of
236 supernatant was collected from cell culture experiments, and spun at 15,000g for 10 minutes to
237 remove debris. Clarified supernatants were aliquoted and frozen before utilizing in ELISA
238 experiments. ELISAs were performed following manufacture protocol without diluting supernatant
239 samples.

240 **3.6 Flow cytometry**

241 Control, SP-R210_L(DN), and SP-R210(KO) RAW 264.7 cells were detached using non-enzymatic cell
242 dissociation medium (Sigma-Aldrich Cat#C1544-100ML) and washed in PBS containing 2% fetal
243 bovine serum (FBS). Cells were washed by centrifugation and discarding of supernatant, then
244 blocked with mouse Fc block (BD Biosciences Cat#553142) in PBS at a concentration of 12.5 μ g/mL
245 and 2% FBS for 10 minutes at room temperature. After blocking, cells were washed and stained
246 with recommended concentrations of monoclonal antibodies for 30 min at 4°C. Staining was divided
247 into two panels; Cells were washed and placed into HBSS with 2% FBS and 0.02% sodium azide until
248 assessment via BD LSRII flow cytometer. A minimum 30,000 events were collected and data were
249 analyzed via FlowJo 9.8.8. Antibodies used are as follows; CD204 (Bio-Rad Cat#MCA1322A488T,
250 2F8); MHC II (eBioscience Cat#86-5321-42, M5/114.15.2); CD11b (BioLegend Cat#101242, M1/70);
251 Ly6C (BD Cat#561237, AL-21); TLR2 (eBioscience Cat#12-9021-82, 6C2); F4/80 (eBioscience Cat#25-

252 4801-82, BM8); CD36 (BD Horizon Cat#585933, CRF D-2712); SIRP α (BD Optibuild Cat#742205, P84);
253 CD11c (eBioscience Cat#17-0114-82, N418); TLR4 (eBioscience Cat#12-9041-80, UT41); CD14
254 (eBioscience Cat#25-0141-82, SA2-8); SiglecF (BD Horizon Cat#562681, E50-2440)

255 **3.7 RNA isolation**

256 RNA was isolated from 1×10^6 cells per sample using the RNA-Bee™ (Tel-Test, Inc. Cat#CS-501B)
257 protocol as described in detail previously (Halstead, et al., 2018). Briefly, plated cells were washed
258 with PBS and 0.5 mL of RNA-Bee Isolation Reagent was added to the cells, lysed with repeated
259 pipetting, and transferred to a microcentrifuge tube followed by the addition of 0.1 mL of
260 chloroform was added, mixed by shaking for 15-30 seconds. and centrifuged at 12,000g for 15
261 minutes at 4°C. The aqueous phase was retained and mixed with 0.5 mL ice-cold isopropanol and
262 placed at -20°C for 3 hours. Samples were then centrifuged at 12,000g for 15 minutes at 4°C and
263 supernatant was discarded. Precipitated RNA was washed with 1 mL ice-cold 75% ethanol twice,
264 and then allowed to air dry for 15-30 minutes at 4°C. RNA was dissolved in 25 μ L RNase, DNase-free
265 deionized water. RNA concentration and purity were determined by NanoDrop (Thermo Scientific)
266 to confirm an A260:A280 ratio above 1.9. RNA integration number (RIN) was measured using
267 BioAnalyzer (Agilent Technologies) RNA 6000 Nano Kit.

268 **3.8 RNA sequencing and analysis**

269 The cDNA libraries were prepared using the NEXTflex™ Illumina Rapid Directional RNA-Seq Library
270 Prep Kit (BioO Scientific) as detailed previously (Halstead, et al., 2018). The libraries were pooled
271 and loaded onto an S1 flow cell on an Illumina NovaSeq 6000 (Illumina) and run for 2X50 cycles at a
272 depth of 25 million reads per sample. De-multiplexed and adapter-trimmed sequencing reads were
273 aligned to the mm10 reference genome using hisat2 (v2.1.0) (Kim, et al., 2015). Abundance for each
274 gene was obtained using featureCounts function available in Rsubread R package (Liao, et al., 2019).
275 The raw count data from 3 independent replicates were analyzed using DESeq2 to obtain
276 differentially expressed genes in uninfected samples, while 2 independent replicates were used for
277 infected experiments (Love, et al., 2014). DESeq2 results were filtered for differentially expressed
278 genes with a p-value of less than 0.05. MGI annotations of immune associated genes were obtained
279 from the gene ontology term 0002376 (<http://www.informatics.jax.org/>). Differentially expressed
280 immune genes were obtained by filtering the DESeq2 results with p-value <0.05 against the MGI

281 database of immune-associated genes. Genes with p-value less than 0.05 were mapped to KEGG
282 pathways using fgsea (Fast Gene Set Enrichment Analysis) package (Kanehisa and Goto, 2000,
283 Korotkevich, et al., 2019). Ingenuity pathway analysis (IPA, www.qiagen.com/ingenuity) was used
284 for upstream pathway analysis of the most highly expressed gene transcripts $q < 0.2$ as measured by
285 Fisher's exact test.

286 **3.9 Chromatin Immunoprecipitation**

287 Five plates each of SP-R210_L(DN) and WT cells were cultured at a density of 1×10^7 for a total of $5 \times$
288 10^7 cells. Cells were removed from the plates and cross-linked for 10 min with 1% formaldehyde in
289 the growth medium. Chromatin was fragmented using the Bioruptor sonicator (Diagenode) for 30
290 min (30s pulses, 30s pauses in between for 10 min, run 3 times) to produce fragments ~ 400 nt in size.
291 ChIP assays were performed as reported by Wang et al. (Wang, et al., 2016). Briefly, 25 μ L of
292 sheared DNA was aliquoted to run as input DNA. anti-PU.1 antibody (50 μ L; Invitrogen Cat #MA5-
293 15064, E.388.3), anti-H3K4me3 (40 μ L; Sigma Aldrich Cat#07-449), anti-H3K9me3 (40 μ L; Abcam
294 Cat#ab8898), or anti-H3K27me3 (40 μ L; Abcam Cat#ab8580) was incubated with 100 μ L of washed
295 Goat-anti-rabbit IgG Dynabeads (Invitrogen Cat#11203D) at 4°C overnight in BSA blocking solution
296 (0.5% BSA in PBS). PU.1 antibody-coated Dynabeads (100 μ L) were incubated with 500 μ L chromatin
297 in TE buffer (with 0.1% deoxycholate, 1% Triton X-100) overnight at 4°C on rotator (Barnstead
298 Labquake Model 4152110). Protein/DNA complexes were washed with RIPA buffer and captured
299 with a Magnetic Particle Concentrator (Invitrogen). DNA-protein crosslink was reversed via
300 incubation at 65°C overnight. Samples were treated with 1 mg/mL proteinase K for 2 hours at 37°.
301 DNA was extracted using phenol and chloroform extraction and precipitated using 100% EtOH. The
302 dried DNA pellet was reconstituted in 50 μ L H₂O treated with 330 μ g/mL of RNase A for 2 hours at
303 37°C and then recovered using the QIAquick PCR Purification kit (QIAGEN Cat#28104). DNA
304 concentration was determined by Qubit (Thermofisher).

305 **3.10 ChIP sequencing and analysis**

306 Libraries of ChIP-derived DNA were sequenced via Illumina NGS. Sequences were aligned to the
307 mm10 genome using the mem function of the bwa package. Peaks were identified from the bed
308 files using the callpeaks function of MACS2 (v2.1.0). Peak annotation and identification of
309 overlapping peaks was done via ChIPpeakAnno (v3.14) using the UCSC mm10 annotated genome

310 (Zhu, et al., 2010). Concordant peaks between the two replicates were selected for further analysis
311 using overlappingPeaks function set at a maxgap=50. Genomic distribution of peaks and pathway
312 analysis was performed using ChIPseeker (v1.16), ReactomePA (v1.24), and clusterProfiler (Yu, et al.,
313 2015, Yu and He, 2016).

314 **3.11 Statistical Analysis**

315 Statistical comparison of data was performed using GraphPad Prism 7.0d software (San Diego, CA).
316 2-way ANOVA with paired samples and unpaired comparisons via *t*-test corrected by the Holm-
317 Sidak method were used to assess statistical differences. *p*-values<0.05 were considered significant.
318

319 **4 Results**

320 **4.1 SP-R210 isoform deficient macrophages exhibit basal immune activation pathways**

321 Previous work has shown that knockdown of the longer SP-R210_L isoform (SP-R210_L(DN))
322 alters cell-surface expression of multiple innate receptor and macrophage differentiation markers
323 (Yang, et al., 2015) (Supplemental Figure 1b). We assessed the impact of SP-R210 isoform deficiency
324 on the basal transcriptome to better understand the phenotypic and functional differences of SP-
325 R210 deficient macrophages. Deseq2 was used on RNA-seq from 3 independent replicates of WT
326 and SP-R210_L(DN) cells to identify differentially expressed genes. This investigation revealed
327 significant differences in the basal transcriptome profile between WT and SP-R210_L(DN). Selective
328 deletion of the SP-R210_L isoform resulted in upregulation of 1273 genes (*p*<0.05), with *Fads2*, *Igf1*,
329 *Runx3*, *Cxcl10*, *Ly86*, *Ifi44*, *Ifi44l* among the top 20 genes with the largest expression differences
330 (Figure 1a, Supplementary Table 1). Furthermore, upregulated genes such as *Hhex* and *Il2rg* were
331 identified by their extremely low *p*-value. Conversely, knockdown of the L isoform resulted in
332 downregulation of 1652 genes, with *Dlg5*, *Maged1*, *Bco1*, *Tmem54*, *Col5a1*, and *Kdm5d* among the
333 top 20 most downregulated genes (Figure 1a, Supplementary Table 1). Other downregulated genes
334 that were identified by noticeably low *p*-values included *Ccl6*, *Lyz1*, *Myo6*, *Stard10*, and *Zcchc24*.
335 Immune associated genes were then identified within the differentially expressed genes by filtering
336 by the gene ontology term GO: 0002376. This filtering identified most of the top upregulated
337 immune associated genes in SP-R210_L(DN) cells, such as *Tnfsf8*, *Ifi44*, *Ifi44l*, *Ly86*, *Runx3*, *Igf1* (Figure

338 1a (red dots), Figure 1b). There were 250 and 211 immune-associated genes that were upregulated
339 and downregulated in SP-R210_L(DN) cells compared to WT cells, respectively.

340 Differentially expressed genes were then analyzed for enrichment in KEGG
341 signaling/metabolism pathways using the fgsea R package. This analysis revealed induction of
342 cytosolic innate recognition pathways for bacteria, RNA and DNA viruses (NOD, RIG-I, and STING,
343 respectively) in SP-R210_L(DN) cells as well as cell-surface and endosomal toll-like receptors (Figure
344 1c, Supplemental Figure 2). Furthermore, several innate sensing pathways (i.e. TLR sensing, NOD
345 sensing) were upregulated in SP-R210_L(DN) cells, which appears to be skewed towards an anti-viral
346 response due to upregulation of cytosolic DNA sensing pathways and RIG-I. Accordingly, the disease
347 associated pathways most upregulated at baseline in SP-R210_L(DN) cells were anti-viral response
348 pathways, including responses to Hepatitis C, Epstein-Barr Virus and Influenza A (Figure 1d).

349 To address the impact of both isoforms, a SP-R210(KO) RAW264.7 macrophage line was
350 generated by CRISPR-Cas9-mediated deletion of both isoforms and expansion of a single clone
351 selected by fluorescence-activated cell sorting (FACS) and deletion confirmed by western blot
352 (Supplemental Figure 1a). Phenotypic analysis by flow cytometry discerned three phenotypes of
353 CD36⁺CD11b⁺F4/80⁺CD14⁺CD204(SR-A)⁺CD284(TLR4)⁺, CD36^{high}CD11b^{high}F4/80^{low}CD14^{high}CD204(SR-
354 A)^{high}CD284(TLR4)^{low}, and CD36^{low}CD11b^{high}F4/80⁺CD14⁺⁺CD204(SR-A)⁺⁺CD284(TLR4)⁺⁺ for WT, SP-
355 R210_L(DN), and SP-R210(KO) cells (Supplemental Figure 1b), respectively. TLR2, SIRPα CD11c, Ly6C,
356 and MHC-II were also highly induced in SP-R210_L(DN) cells while only moderately elevated in SP-
357 R210(KO) cells compared to WT (Supplemental Figure 1b).

358 Comparative analysis of RNAseq data revealed that disruption of L and both L and S isoforms
359 results in widespread transcriptome adaptation affecting both immune and nonimmune genes. 804
360 genes were upregulated and 778 downregulated in SP-R210(KO) cells compared to WT. *Tnfrsf4*,
361 *Plch1*, *Amer3*, and *Cxcl10* were among the top 20 upregulated genes in the SP-R210(KO) cells, while
362 *Maged1*, *Zfmx4*, *Cldn11*, and *Csf1* were among the 20 most downregulated genes (Supplemental
363 Figure 1c, Supplemental Table 1). Compared to SP-R210_L(DN) cells, 1936 genes were upregulated
364 while 1525 genes were downregulated in SP-R210(KO) cells compared to SP-R210_L(DN) cells.
365 Upregulated genes included *Bco1*, *Tmem54*, *Ifi272b*, and *Kdm5d*, while *Ly86*, *Igf1*, *Fads2*, *Runx3*,
366 *Ifi44*, *Csf1*, *Ifi44l*, and CD86 were among the top 20 downregulated genes (Supplemental Figure 1d,
367 Supplemental Table 1). *Ly86*, *Ifi44*, *Ifi44l*, *Runx3*, and *Fads2* were all among the top 20 genes that
368 were downregulated in both WT and SP-R210(KO) cells compared to SP-R210_L(DN) cells.

369 Furthermore, 224 transcripts common to both SP-R210_L(DN) and SP-R210(KO) were downregulated
370 while 596 genes were upregulated in both cell types compared to WT cells (Supplemental Figure 1g)
371 and of these, 171 upregulated and 101 downregulated transcripts are from immune-associated
372 genes. Among the top 20 upregulated genes in SP-R210(KO) cells, only *Tnfsf4*, *Itga2*, *Ifi2712b*, and
373 *Cxcl10* were immune-associated compared to WT cells (Supplemental Figure 1c, red dots). *Tnfsf4*
374 and *Ifi2712b* remained elevated in SP-R210(KO) cells to SP-R210_L(DN) cells (Supplemental Figure 1d,
375 red dots). KEGG pathway analysis showed that only RIG-I and NOD-like receptor signaling pathways
376 remained elevated SP-R210(KO) compared to WT cells (Supplemental Figure 1e, 1f), whereas
377 nucleic acid sensing pathways were not affected. Taken together, these findings indicate basal
378 macrophage activation readiness at the transcriptional level depends on differential expression of
379 SP-R210 isoforms.

380 **4.2 Depletion of SP-R210_L alters genome wide binding of PU.1**

381 To further understand the impact of L depletion, chromatin immunoprecipitation and
382 sequencing (ChIP-seq) was used to determine the genome-wide distribution of PU.1 binding in WT
383 and SP-R210_L(DN) cells. PU.1, a pioneer transcription factor, plays a key role in macrophage function
384 and lineage through its interaction with a constellation of transcription factors at distal gene
385 enhancer and proximal promoter elements, allowing it to prime expression of various macrophage
386 and immune associated genes (Shibata, et al., 2001, Glass and Natoli, 2016, Hoogenkamp, et al.,
387 2007, Imperato, et al., 2015, Petrovick, et al., 1998, Schmidt, et al., 2016, Berclaz, et al., 2007). ChIP-
388 seq was performed on two independent samples for each cell type; concordant peaks were
389 identified between both replicates and were used for further analysis. Comparative analysis of ChIP-
390 seq peaks showed that the number of PU.1 binding sites increased in SP-R210_L(DN) cells compared
391 to WT (Figure 2a). Furthermore, ChIPseeker analysis revealed that SP-R210_L(DN) cells had a greater
392 distribution of PU.1 binding in introns than in WT cells (34.64 % vs 33.57%, respectively (Figure 2b).
393 Conversely, binding in promoter regions and regions downstream of gene transcriptional start sites
394 decreased in SP-R210_L(DN) compared to WT cells (24.94 vs 26.11%, respectively) (Figure 2b).
395 Differences in PU.1 binding were not due to differences in PU.1 expression levels, as demonstrated
396 by Western blot analysis (Supplemental Figure 2a, 2b). These results indicate that knockdown of SP-
397 R210_L shifts the distribution of PU.1 binding sites between intergenic and proximal gene promoter
398 sites.

399 The PU.1 peaks were annotated using ChIPseeker, to associate the peaks to specific genes. Of
400 the 1320 peaks unique to WT cells, 260 of the peaks were associated with transcripts
401 downregulated in SP-R210_L(DN) cells, while 49 peaks were associated with upregulated transcripts
402 in SP-R210_L(DN) cells. Of the 5365 peaks unique to SP-R210_L(DN) cells, 573 were associated with
403 upregulated transcripts in the knockdown cells, while 437 were associated with downregulated
404 transcripts in the knockdown cells (Supplemental Table 2a, Supplemental Figure 3). Additionally, of
405 the 1273 upregulated genes in SP-R210_L(DN) cells, 363 had PU.1 peaks that were found exclusively
406 in SP-R210_L(DN) cells, with 44 genes having PU.1 peaks exclusive to WT cells. Within the 1652
407 downregulated genes, 226 genes had PU.1 peaks unique to WT cells, while 308 genes had PU.1
408 peaks unique to the SP-R210_L(DN) cells (Figure 2c). Of note, upregulated SP-R210_L(DN) genes that
409 had PU.1 peaks unique to these cells include several immune associated genes, such as *Ly86*, *Csf3r*,
410 *Pde8a*, and *Igf1*, as well as epigenetic regulators such as *Hdac9* (Supplemental Table 2a). On the
411 other hand, downregulated SP-R210_L(DN) genes that associated with unique PU.1 peaks in the
412 knockdown cells include genes involved in signaling, such as *Marcks*, *Rgs9*, *Fgr* and *Plekha6*
413 (Supplemental Table 2b).

414 We then used the ReactomePA package to map gene regions immunoprecipitated by PU.1 to
415 Reactome pathways and clusterProfiler to determine pathway clustering. This analysis showed
416 enrichment in pathways involved in macrophage function in both WT and SP-R210_L(DN) cells.
417 Pathways regulating Fc gamma receptor dependent phagocytosis, genes regulating actin dynamics
418 for phagocytic cup formation, as well as other immune associated pathways, such as IL-3,5 and GM-
419 CSF signaling, and CD28 co-stimulation pathways (Supplemental Figure 4). SP-R210_L(DN) cells,
420 however, showed an increased representation of genes involved in TLR pathways (Figure 2d,
421 Supplemental Figure 5), consistent with the RNA-seq data showing differential expression of
422 transcripts associated with TLR signaling (Figure 1b). Other pathways include genes involved in TNF,
423 interferon, Fc epsilon receptor, and NLR signaling pathways. Cyclin D associated events in G1, and
424 transcriptional regulation of TP53 were also differentially bound by PU.1 binding in SP-R210_L(DN)
425 cells (Supplemental Figure 4).

426 **4.3 Differential distribution of histone methylation marks in WT and SP-R210_L(DN) cells**

427 Previous studies reported that PU.1 binding is influenced by histone 3 (H3) methylation
428 (Cheng, et al., 2013, Burda, et al., 2016, Tagore, et al., 2015). Methylation marks on lysine residues

429 of histone 3 (H3) are associated with certain chromatin conformations; H3K4me3 with open
430 chromatin and transcriptional activity, and H3K9me3 and H3K27me3 are typically associated with
431 closed chromatin and thus transcriptional suppression. Profiling of by ChIP-seq showed increased
432 H3K4 trimethylation (H3K4me3) in SP-R210_L(DN) cells compared to WT cells (Figures 3a, 3b).
433 Conversely, methylation marks associated with transcriptional repression, H3K9 trimethylation
434 (H3K9me3), and H3K27 trimethylation (H3K27me3), were decreased in SP-R210_L(DN) cells
435 compared to WT cells (Figures 3c, 3d, 3e, and 3f). The distribution of these methylation marks was
436 also altered around specific genomic features in SP-R210_L(DN) cells with decreased distribution of
437 H3K4me3 marks in promoter regions, whereas H3K4me3 was higher in introns and intergenic
438 regions (Figure 3b). The H3K4me3 methylation pattern overlapped with 23.5% and 34.9% of PU.1
439 binding sites representing 1911 regions in WT cells and 10413 in SP-R210_L(DN) cells (Figure 3g, 3h),
440 respectively.

441 Plotting of bedgraphs on the UCSC browser was used to examine the relationship between
442 PU.1 binding and histone methylation pattern for TLR genes, since TLR response pathways were
443 differentially affected in SP-R210_L(DN) cells. Concordant peaks for both PU.1 and H3K4me3 in the
444 promoter regions of *Tlr3*, *5*, *6*, and *9* were broad and narrow in WT and SP-R210_L(DN) cells,
445 respectively. However, there were additional and/or shifted peaks for PU.1 and H3K4me3 near the
446 transcriptional start site of *Tlr2*, *Tlr5*, *Tlr6*, *Tlr9* and *Tlr13* in SP-R210_L(DN) cells (red arrows,
447 Supplemental Figure 5). Sharp PU.1 peaks near or further upstream the transcriptional start site for
448 *Tlr4* and *Tlr7* were not different between WT and SP-R210_L(DN) cells, and these peaks were not
449 concordant to H3K4me3 (Figure 4a, Supplemental Figure 5). There were no discernible PU.1 or
450 H3K4me3 peaks for *Tlr1*, *Tlr3*, *Tlr8*, *Tlr11* and *Tlr12* (Supplemental Figures 6). Narrow PU.1 peaks at
451 sites distal to the promoter of *Tlr13* were discernible only in SP-R210_L(DN) regions and these peaks
452 were concordant to H3K4me3 (Supplemental Figure 5). Validating our immunoprecipitation
453 experiment, PU.1 binding was identified at the known enhancer binding site upstream of the PU.1
454 transcriptional start site in both WT and SP-R210_L(DN) cells (Figure 4b). A low intensity PU.1 peak in
455 the proximal PU.1 promoter was retained in WT but not SP-R210_L(DN) cells, whereas a broad
456 H3K4Me3 peak was present in both (Figure 4b). By comparison, chromatin peak analysis of the
457 *Csfr1* gene revealed broad and narrow PU.1 and H3K4Me3 peaks downstream of the first exon in
458 WT and SP-R210_L(DN) cells, respectively (Supplemental Figure 5). Bedgraph analysis of the *Myo18A*
459 gene encoding SP-R210 isoforms revealed two consensus PU.1 binding motifs in the reverse

460 complement and forward strand orientations (Figure 4c). Of these, only the intronic cis site was
461 occupied by PU.1 in both WT and SP-R210_L(DN) cells. An additional non-consensus PU.1 binding
462 peak was present upstream in the same intron, suggesting indirect PU.1 binding at this site.
463 Sequence analysis of these peaks revealed a canonical PU.1 binding sequence near the intronic peak,
464 while a non-canonical PU.1 binding motif was identified by UCI motifmap near the upstream site (K,
465 et al., 2011, G, et al., 2013, V, 2016). A sharp H3K4Me3 peak in the promoter region had reduced
466 intensity in SP-R210_L(DN) cells (Figure 4c).

467 **4.4 IAV infection results in repression and redistribution of PU.1 binding and differential** 468 **outcomes of cellular death and signaling responses in WT and SP-R210_L(DN) cells**

469 PU.1 is critical for the terminal differentiation of alveolar macrophages downstream from GM-
470 CSF receptor signaling in the local microenvironment (Carey, et al., 2007). In turn, alveolar
471 macrophages are essential for host survival from severe influenza A virus (IAV) infection (Halstead,
472 et al., 2018, Sever-Chroneos, et al., 2011, Umstead, et al., 2020, Huang, et al., 2011). Raw264.7 cells
473 have been extensively utilized as a surrogate *in vitro* model to study IAV infection in macrophages
474 with all known IAV strains (Marvin, et al., 2017, Cline, et al., 2017). Infection of IAV in macrophages
475 is largely abortive, whereby replication, transcription, and translation of viral genes takes place with
476 minimal packaging and release of viral progeny (Marvin, et al., 2017, Cline, et al., 2017). Therefore,
477 we asked whether IAV infection on alters PU.1 chromatin occupancy in WT and SP-R210_L(DN) cells.
478 IAV infection and lack of the L isoform did not alter PU.1 expression WT and SP-R210_L(DN) cells
479 (Supplemental Figure 3). ChIP-seq immunoprecipitation experiments revealed that IAV infection
480 reduced PU.1 binding by almost 40 and 65%, respectively, compared to uninfected cells (Figure 5a,
481 5b). The SP-R210_L(DN) genome had 3153 fewer PU.1 peaks compared to uninfected cells, whereas
482 the number of PU.1 peaks in SP-R210_L(DN) cells decreased by 7560 compared to uninfected cells
483 (Figure 5a). Of these, 733 and 197 PU.1 peaks were uniquely associated with infection in WT and SP-
484 R210_L(DN) cells, respectively (Figure 5b). Mapping of these unique peak regions showed increased
485 distribution of PU.1 peaks in proximal promoter regions by 7 and 3.3%, or a 2-fold difference
486 between infected WT and SP-R210_L(DN) cells, respectively. The 2-fold increase reflected lower PU.1
487 distribution in intronic and distal intergenic regions in WT cells compared to lower distribution in
488 intronic regions in SP-R210_L(DN) cells (Figure 5c). PU.1 peaks in shared genomic regions mapped to
489 mostly macrophage function and activation pathways (e.g. Fc gamma receptor dependent

490 phagocytosis, regulation of actin dynamics for phagocytosis, clathrin-mediated endocytosis, and
491 signaling by RHO GTPases) in both WT and SP-R210_L(DN) cells (Figure 5d, Supplemental Figure 8)
492 and these were selectively suppressed after infection of SP-R210_L(DN) cells. IAV infection, however,
493 resulted in differential increase in association of PU.1 with genes regulating apoptotic and
494 hyaluronan metabolism pathways, whereas binding to genes associated with proinflammatory TLR
495 pathways decreased in WT and SP-R210_L(DN) cells, respectively (Figure 5d, Supplemental Figure 10).
496 Accordingly, flow cytometric experiments confirmed the pro-apoptotic phenotype of WT cells and
497 resistance to apoptosis in response to IAV infection in WT and WT and SP-R210_L(DN) cells,
498 respectively (Supplemental Figure 9a) and activation of apoptotic, cell death, and sirtuin pathways
499 (Supplemental Figure 9b). On the other hand, phosphorylation of IRF3 and IRF7 were both
500 enhanced by 12 and 24 hrs after IAV infection in SP-R210_L(DN) cells compared to WT (Figure 6a, b),
501 consistent with enhancement of interferon and TLR signaling pathways. IAV infection increased
502 Furthermore, expression of TLR7 but not TLR4 (Supplemental Figure 10) in SP-R210_L(DN) cells
503 compared to WT. Analysis of NFκB p65 phosphorylation revealed basal increase in the levels of
504 serine 276 which remained elevated after infection in SP-R210_L(DN) cells (Figure 6c), whereas
505 phosphorylation of serine 536 was differentially induced in WT cells. Given that serine 536
506 phosphorylation is involved in negative regulation of NFκB signaling (Pradere, et al., 2016), we
507 assessed phosphorylation of the upstream p65 kinase p38 (Song, et al., 2006, Schmeck, et al., 2004).
508 Accordingly, Figure 8d shows that IAV infection induced phosphorylation of p38 in WT but not SP-
509 R210_L(DN) cells (Figure 6d). This difference aligns with the decrease in PU.1 binding to genes that
510 regulate MAPK signaling (Figure 5d).

511 **5 Discussion**

512 This study explored how SP-R210 isoforms coordinate macrophage transcriptional and
513 epigenetic regulation of macrophage function. We report that depletion of the L isoform switches
514 macrophages to a primed state marked by heterochromatin reduction accelerating responses to
515 inflammatory and infectious stimuli. Previous studies showed that selective disruption of SP-R210_L
516 in macrophages alters activation state coupled to changes in trafficking and expression of
517 phenotypic markers of macrophage activation and differentiation, encompassing pattern
518 recognition, scavenger, and adhesion receptors enhancing phagocytic function and responsiveness
519 to inflammatory and infectious stimuli extrinsic ligand-independent functions of SP-R210 that

520 depend on relative abundance of SP-R210 isoforms (Yang, et al., 2015, Yang, et al., 2005, Sever-
521 Chroneos, et al., 2011). Here, we extend upon these findings, showing that selective disruption of
522 the L isoform results in broad priming and activation of antiviral response pathways and chromatin
523 accessibility and remodeling as demonstrated by transcriptome analysis and chromatin
524 immunoprecipitation experiments. Additionally, disruption of both isoforms appears to result in an
525 intermediate phenotype marked by normalization of most cell-surface markers examined and
526 moderate anti-viral response to influenza infection compared to WT and SP-R210_L(DN) cells,
527 supporting that the L and S isoforms modulate antagonistic extremes of macrophage. inflammatory
528 and anti-inflammatory activation states in part through a signaling mechanism that modulates PU.1-
529 dependent chromatin remodeling.

530 Transcriptome data support the novel hypothesis that L-deficient macrophages undergo
531 metabolic, transcriptional, and epigenetic adaptation related to lipid and fatty acid uptake,
532 utilization, and metabolism to be addressed in future studies. Thus, it is noteworthy that expression
533 of fatty acid uptake and metabolism genes *Fads2* and *Igf1* mRNA, and cell-surface CD36 and SR-A
534 proteins (Oishi, et al., 2017, Koundouros and Pouligiannis, 2020, Cucchi, et al., 2019, Spadaro, et al.,
535 2017) were highly induced in uninfected SP-R210_L(DN) cells. In contrast, deletion of both isoforms
536 diminished cell-surface expression of CD36. Phenotypic expression level of CD36 distinguished anti-
537 inflammatory from inflammatory macrophages in human adipose tissue based on diminished and
538 high CD36 expression, respectively (Kralova Lesna, et al., 2016). It is also noteworthy that histone
539 deacetylase 9 (*Hdac9*), a deacetylase for histones, transcription factors, and other signaling
540 molecules, was highly induced in SP-R210_L(DN) cells. HDAC9 is one of several deacetylases that
541 promote inflammatory M1 macrophage polarization by repressing nuclear receptors and
542 cholesterol efflux (Cao, et al., 2014). Furthermore, deacetylation of the interferon regulating kinase
543 TBK1 by HDAC9 was shown to enhance production of Type I interferon augmenting antiviral activity
544 (Li, et al., 2016), consistent with the basal anti-viral phenotype of the L-deficient macrophages.
545 Accordingly, TBK1 and related antiviral control genes were induced in SP-R210_L(DN) cells after IAV
546 infection, whereas the infection resulted in apoptotic and sirtuin pathway involvement in WT cells.
547 Sirtuins respond to cellular NAD⁺/NADH redox balance bioavailability, thereby targeting a broad
548 range of protein substrates that drive apoptosis, DNA repair, metabolism, and inflammation in
549 response to different cellular conditions (Zhang and Sauve, 2018).

550 The global transcriptome adaptation of the L-deficient cells was accompanied by differences
551 in accessibility of the transcription factor PU.1 and chromatin remodeling as demonstrated by
552 increased genome-wide deposition of PU.1 and epigenetic histone modification. The pattern of
553 histone methylation marks is consistent with increased activation state of SP-R210_L(DN) cells as
554 indicated by increased number of genes associated with H3K4me3 compared to decreases in
555 H3K9me3 and H3K27me3 associated chromatin, although in all cases there was marked
556 redistribution of these trimethylated histones from promoter to non-promoter regions. As a
557 pioneer transcription factor, PU.1 interacts with both promoter and non-promoter regions
558 throughout the genome in both active and repressive chromatin, regulating chromatin accessibility
559 and gene expression. PU.1 maintains chromatin at an open conformation to allow binding of
560 stimulus-dependent transcription factors and elicit expression of macrophage activation genes by
561 displacing nucleosomes, whereas tight control of PU.1 levels plays a critical role in the fate of
562 hematopoietic stem cells towards myeloid or lymphocytic lineages. On the other hand, chromatin
563 structure and composition of methylated and acetylated histones may limit PU.1 access in closed
564 transcriptionally inactive chromatin after lineage commitment (Glass and Natoli, 2016,
565 Hoogenkamp, et al., 2007, Imperato, et al., 2015, Petrovick, et al., 1998, Schmidt, et al., 2016,
566 Karpurapu, et al., 2011, Liu and Ma, 2006, Rosa, et al., 2007, Celada, et al., 1996, Ha, et al., 2019,
567 Qian, et al., 2015, Rothenberg, et al., 2019, Ghisletti, et al., 2010, van Riel and Rosenbauer, 2014,
568 Leddin, et al., 2011). The number of PU.1 peaks in active chromatin enriched in H3K4Me3 increased
569 five-fold in L-deficient cells, indicating marked reconfiguration of chromatin of the SP-R210_L(DN) cell
570 genome from a closed to an active state, although additional DNA accessibility studies are needed
571 to validate this finding. Lack of L did not have a major impact on the overall fractional distribution of
572 PU.1 between promoter and non-promoter binding sites in uninfected cells. Selective analysis of
573 PU.1 bound genes revealed sharp PU.1 peaks near transcriptional start sites in SP-R210_L(DN) cells
574 compared to the broad heterogeneous PU.1 peaks, or a complete absence of peaks, in WT cells at
575 proximal intronic regions downstream from the transcriptional start site in several but not all TLR
576 genes (*Tlr3, 5, 6, 9, and 13*). Analysis of the TATA-less *Csfr1*, a known PU.1 regulated gene, displayed
577 similar repositioning as seen with narrow PU.1 binding peaks in the known PU.1 intronic binding
578 sites in this gene. In contrast, the shape of the PU.1 peaks in the enhancer regions -15 to -8 kb
579 upstream the PU.1 promoter (van Riel and Rosenbauer, 2014, Leddin, et al., 2011) were not
580 affected. PU.1 binding consensus motifs were identified inside the first intron and upstream near

581 the transcriptional start site on the opposite strand of the Myo18A gene, although only the intronic
582 site was occupied in a sharp PU.1 peak and this was similar in both WT and SP-R210_L(DN) cells.
583 Whether this PU.1 site contributes to expression for the L isoform in mature macrophages but not
584 macrophage precursors remains to be determined. Therefore, downregulation of the L isoform
585 alters local positioning and complexity of intragenic PU.1 binding and association with promoter
586 and intronic elements.

587 In response to IAV infection, however, there was marked expulsion of PU.1 binding,
588 depleting PU.1 from genes affecting diverse regulatory processes in WT cells but predominantly
589 macrophage activation genes regulating toll-like receptor signaling in SP-R210_L(DN) cells.
590 Assessment of bound PU.1 showed increased distribution of PU.1 promoter sites associated with
591 activation of cellular death pathways and metabolism in WT and SP-R210_L(DN) cells. The SP-
592 R210_L(DN) cells, however, retained the ability to elaborate anti-viral responses to IAV infection.
593 These findings support the model that depletion of SP-R210_L results in PU.1-dependent
594 heterochromatin reduction and basal activation of SP-R210_{L-S+} macrophages priming macrophage
595 activation through differential regulation of p38 and NFκB pathways and activation of IRF3/7
596 signaling in response to influenza infection.

597

598 **6 Conclusion**

599 This study explored how SP-R210 isoforms coordinate macrophage transcriptional and
600 epigenetic regulation of macrophage function. We report that depletion of the L isoform switches
601 macrophages to a primed state marked by associated heterochromatin reduction that was
602 accompanied by redistribution and expansion of PU.1 chromatin occupancy. This chromatin
603 remodeling may accelerate responses to inflammatory and infectious stimuli. To this end, the
604 mechanisms that elicit PU.1 redistribution and heterochromatin reduction in macrophages and
605 other immune cells are only partly understood (Tagore, et al., 2015, Minderjahn, et al., 2020,
606 McAndrew, et al., 2016). On the other hand, decline in expression of the L isoform alters SP-A
607 binding from linear non-cooperative to binding with positive cooperative behavior (Supplemental
608 Figure 11a and b) in WT and SP-R210_L(DN) cells, respectively. In this regard, future studies are
609 needed to elucidate the cross-talk between SP-A and GM-CSF (Shibata, et al., 2001, Chroneos and
610 Shepherd, 1995, Blau, et al., 1994, Yoshida, et al., 2001), its role modulating alveolar macrophage

611 function and local homeostasis, and whether PU.1 is the downstream effector of this interaction *in*
612 *vivo*. This may contribute to dynamic modulation of immune activation threshold of alveolar and
613 inflammatory macrophages with different expression of SP-R210 isoforms to modulate
614 inflammation and host resistance to infection. Our study provides the framework for further studies
615 to delineate intrinsic and ligand-dependent mechanisms by which SP-R210 isoforms in macrophages
616 regulate homeostatic and inflammatory functions of resident macrophage populations.

617

618

619 **7 Conflict of Interest**

620 Zissis C. Chroneos is co-founder of Respana Therapeutic, Inc. (<http://respana-therapeutics.com/>) an
621 early-stage company developing therapeutics targeting SP-R210 isoforms.

622

623 **8 Author Contributions**

624 EY acquired, analyzed, graphed genomic data, and wrote the manuscript. YC and EY developed and
625 performed influenza infection assays and processed cells for RNAseq analysis. CS provided expertise
626 for chromatin immunoprecipitation experiments. JW produced and isolated SP-R210(KO) data using
627 CRISPR. YIA oversaw the generation of RNAseq and ChIP-derived libraries, acquisition RNAseq and
628 ChIPseq data, provided expertise for bioinformatics analysis, and read manuscript critically. ZT and
629 YT provided expertise and reagents for CRISPR knockout of SP-R210. TMU purified IAV, performed
630 experiments, and edited manuscript. SD provided reagents and expertise in analysis of epigenetic
631 data. ZC conceptualized, designed, contributed to bioinformatics analysis, led the study, and co-
632 wrote the manuscript.

633

634 **9 Funding**

635 This work was funded in part by PHS grants HL128746, Pennsylvania Department of Health The
636 Children's Miracle Network, and the Department of Pediatrics Pennsylvania State University College
637 of Medicine.

638

639 **10 Acknowledgments**

640 We would like to thank Nate Schaffer and Joseph Bednarzyk from the Pennsylvania State University
641 College of Medicine Flow Cytometry Core Facility as well as the Institute of Personalized Medicine
642 for assistance with flow cytometry and genomic processes.

643

644 **11 References**

- 645 Sica, A., Mantovani, A. 2012. Macrophage plasticity and polarization: in vivo veritas. *J Clin Invest* 122,
646 787.
- 647 Italiani, P., Boraschi, D. 2014. From Monocytes to M1/M2 Macrophages: Phenotypical vs. Functional
648 Differentiation. *Front Immunol* 5, 514.
- 649 Stout, R.D., Jiang, C., Matta, B., Tietzel, I., Watkins, S.K., Suttles, J. 2005. Macrophages sequentially
650 change their functional phenotype in response to changes in microenvironmental influences.
651 *J Immunol* 175, 342.
- 652 Hussell, T., Bell, T.J. 2014. Alveolar macrophages: plasticity in a tissue-specific context. *Nat Rev*
653 *Immunol* 14, 81.
- 654 McQuattie-Pimentel, A.C., Ren, Z., Joshi, N., Watanabe, S., Stoeger, T., Chi, M., Lu, Z., Sichizya, L.,
655 Aillon, R.P., Chen, C.I., Soberanes, S., Chen, Z., Reyfman, P.A., Walter, J.M., Anekalla, K.R.,
656 Davis, J.M., Helmin, K.A., Runyan, C.E., Abdala-Valencia, H., Nam, K., Meliton, A.Y., Winter,
657 D.R., Morimoto, R.I., Mutlu, G.M., Bharat, A., Perlman, H., Gottardi, C.J., Ridge, K.M.,
658 Chandel, N.S., Sznajder, J.I., Balch, W.E., Singer, B.D., Misharin, A.V., Budinger, G.R.S. 2021.
659 The lung microenvironment shapes a dysfunctional response of alveolar macrophages in
660 aging. *J Clin Invest* 131.
- 661 Upham, J.W., Strickland, D.H., Bilyk, N., Robinson, B.W., Holt, P.G. 1995. Alveolar macrophages from
662 humans and rodents selectively inhibit T-cell proliferation but permit T-cell activation and
663 cytokine secretion. *Immunology* 84, 142.
- 664 Kobzik, L., Godleski, J.J., Brain, J.D. 1990. Selective down-regulation of alveolar macrophage
665 oxidative response to opsonin-independent phagocytosis. *J Immunol* 144, 4312.
- 666 Shibata, Y., Berclaz, P.Y., Chroneos, Z.C., Yoshida, M., Whitsett, J.A., Trapnell, B.C. 2001. GM-CSF
667 regulates alveolar macrophage differentiation and innate immunity in the lung through PU.1.
668 *Immunity* 15, 557.
- 669 Baker, A.D., Malur, A., Barna, B.P., Ghosh, S., Kavuru, M.S., Malur, A.G., Thomassen, M.J. 2010.
670 Targeted PPAR γ deficiency in alveolar macrophages disrupts surfactant catabolism.
671 *Journal of lipid research* 51, 1325.
- 672 Chroneos, Z.C., Sever-Chroneos, Z., Shepherd, V.L. 2010. Pulmonary surfactant: an immunological
673 perspective. *Cell Physiol Biochem* 25, 13.
- 674 Guilliams, M., De Kleer, I., Henri, S., Post, S., Vanhoutte, L., De Prijck, S., Deswarte, K., Malissen, B.,
675 Hammad, H., Lambrecht, B.N. 2013. Alveolar macrophages develop from fetal monocytes
676 that differentiate into long-lived cells in the first week of life via GM-CSF. *J Exp Med* 210,
677 1977.

- 678 Bates, S.R., Xu, J., Dodia, C., Fisher, A.B. 1997. Macrophages primed by overnight culture
679 demonstrate a marked stimulation of surfactant protein A degradation. *Am J Physiol* 273,
680 L831.
- 681 Schneider, C., Nobs, S.P., Kurrer, M., Rehrauer, H., Thiele, C., Kopf, M. 2014. Induction of the nuclear
682 receptor PPAR-gamma by the cytokine GM-CSF is critical for the differentiation of fetal
683 monocytes into alveolar macrophages. *Nat Immunol* 15, 1026.
- 684 Tan, S.Y., Krasnow, M.A. 2016. Developmental origin of lung macrophage diversity. *Development*
685 143, 1318.
- 686 He, W., Chen, C.J., Mullarkey, C.E., Hamilton, J.R., Wong, C.K., Leon, P.E., Uccellini, M.B., Chromikova,
687 V., Henry, C., Hoffman, K.W., Lim, J.K., Wilson, P.C., Miller, M.S., Krammer, F., Palese, P., Tan,
688 G.S. 2017. Alveolar macrophages are critical for broadly-reactive antibody-mediated
689 protection against influenza A virus in mice. *Nat Commun* 8, 846.
- 690 Kirby, A.C., Coles, M.C., Kaye, P.M. 2009. Alveolar macrophages transport pathogens to lung
691 draining lymph nodes. *J Immunol* 183, 1983.
- 692 Roth, M.D., Golub, S.H. 1993. Human pulmonary macrophages utilize prostaglandins and
693 transforming growth factor beta 1 to suppress lymphocyte activation. *J Leukoc Biol* 53, 366.
- 694 Schneider, C., Nobs, S.P., Heer, A.K., Kurrer, M., Klinke, G., van Rooijen, N., Vogel, J., Kopf, M. 2014.
695 Alveolar macrophages are essential for protection from respiratory failure and associated
696 morbidity following influenza virus infection. *PLoS Pathog* 10, e1004053.
- 697 Purnama, C., Ng, S.L., Tetlak, P., Setiagani, Y.A., Kandasamy, M., Baalashubramanian, S., Karjalainen,
698 K., Ruedl, C. 2014. Transient ablation of alveolar macrophages leads to massive pathology of
699 influenza infection without affecting cellular adaptive immunity. *Eur J Immunol* 44, 2003.
- 700 Halstead, E.S., Umstead, T.M., Davies, M.L., Kawasawa, Y.I., Silveyra, P., Howyrlak, J., Yang, L., Guo,
701 W., Hu, S., Hewage, E.K., Chroneos, Z.C. 2018. GM-CSF overexpression after influenza a virus
702 infection prevents mortality and moderates M1-like airway monocyte/macrophage
703 polarization. *Respir Res* 19, 3.
- 704 Halstead, E.S., Chroneos, Z.C. 2015. Lethal influenza infection: Is a macrophage to blame? *Expert*
705 *Rev Anti Infect Ther*, 1.
- 706 Casals, C., Garcia-Fojeda, B., Minutti, C.M. 2019. Soluble defense collagens: Sweeping up immune
707 threats. *Mol Immunol* 112, 291.
- 708 Minutti, C.M., Knipper, J.A., Allen, J.E., Zaiss, D.M. 2017. Tissue-specific contribution of
709 macrophages to wound healing. *Semin Cell Dev Biol* 61, 3.
- 710 Canadas, O., Olmeda, B., Alonso, A., Perez-Gil, J. 2020. Lipid-Protein and Protein-Protein
711 Interactions in the Pulmonary Surfactant System and Their Role in Lung Homeostasis. *Int J*
712 *Mol Sci* 21.
- 713 Autilio, C., Perez-Gil, J. 2019. Understanding the principle biophysics concepts of pulmonary
714 surfactant in health and disease. *Arch Dis Child Fetal Neonatal Ed* 104, F443.
- 715 Nguyen, H.A., Rajaram, M.V., Meyer, D.A., Schlesinger, L.S. 2012. Pulmonary surfactant protein A
716 and surfactant lipids upregulate IRAK-M, a negative regulator of TLR-mediated inflammation
717 in human macrophages. *Am J Physiol Lung Cell Mol Physiol* 303, L608.
- 718 Phelps, D.S., Umstead, T.M., Silveyra, P., Hu, S., Wang, G., Floros, J. 2013. Differences in the alveolar
719 macrophage proteome in transgenic mice expressing human SP-A1 and SP-A2. *J Proteom*
720 *Genom Res* 1, 2.
- 721 Phelps, D.S., Umstead, T.M., Quintero, O.A., Yengo, C.M., Floros, J. 2011. In vivo rescue of alveolar
722 macrophages from SP-A knockout mice with exogenous SP-A nearly restores a wild type
723 intracellular proteome; actin involvement. *Proteome Sci* 9, 67.

- 724 Minutti, C.M., Garcia-Fojeda, B., Saenz, A., de Las Casas-Engel, M., Guillamat-Prats, R., de Lorenzo,
725 A., Serrano-Mollar, A., Corbi, A.L., Casals, C. 2016. Surfactant Protein A Prevents IFN-
726 gamma/IFN-gamma Receptor Interaction and Attenuates Classical Activation of Human
727 Alveolar Macrophages. *J Immunol* 197, 590.
- 728 Francisco, D., Wang, Y., Conway, M., Hurbon, A.N., Dy, A.B.C., Addison, K.J., Chu, H.W., Voelker, D.R.,
729 Ledford, J.G., Kraft, M. 2020. Surfactant Protein-A Protects against IL-13-Induced
730 Inflammation in Asthma. *J Immunol* 204, 2829.
- 731 Younis, U.S., Chu, H.W., Kraft, M., Ledford, J.G. 2020. A 20-mer peptide derived from the lectin
732 domain of SP-A2 decreases TNF-alpha production during *Mycoplasma pneumoniae* infection.
733 *Infect Immun*.
- 734 Moulakakis, C., Steinhäuser, C., Biedziak, D., Freundt, K., Reiling, N., Stamme, C. 2016. Surfactant
735 Protein A Enhances Constitutive Immune Functions of Clathrin Heavy Chain and Clathrin
736 Adaptor Protein 2. *Am J Respir Cell Mol Biol* 55, 92.
- 737 Moulakakis, C., Stamme, C. 2009. Role of clathrin-mediated endocytosis of surfactant protein A by
738 alveolar macrophages in intracellular signaling. *Am J Physiol Lung Cell Mol Physiol* 296, L430.
- 739 Wu, Y., Adam, S., Hamann, L., Heine, H., Ulmer, A.J., Buwitt-Beckmann, U., Stamme, C. 2004.
740 Accumulation of inhibitory kappaB-alpha as a mechanism contributing to the anti-
741 inflammatory effects of surfactant protein-A. *Am J Respir Cell Mol Biol* 31, 587.
- 742 Henning, L.N., Azad, A.K., Parsa, K.V., Crowther, J.E., Tridandapani, S., Schlesinger, L.S. 2008.
743 Pulmonary Surfactant Protein A Regulates TLR Expression and Activity in Human
744 Macrophages. *J Immunol* 180, 7847.
- 745 Gil, M., McCormack, F.X., Levine, A.M. 2009. Surfactant protein-A modulates cell surface expression
746 of CR3 on alveolar macrophages and enhances CR3-mediated phagocytosis. *J Biol Chem*.
- 747 Yang, L., Carrillo, M., Wu, Y.M., DiAngelo, S.L., Silveyra, P., Umstead, T.M., Halstead, E.S., Davies,
748 M.L., Hu, S., Floros, J., McCormack, F.X., Christensen, N.D., Chroneos, Z.C. 2015. SP-R210
749 (Myo18A) Isoforms as Intrinsic Modulators of Macrophage Priming and Activation. *PLoS One*
750 10, e0126576.
- 751 Weikert, L.F., Lopez, J.P., Abdolrasulnia, R., Chroneos, Z.C., Shepherd, V.L. 2000. Surfactant protein
752 A enhances mycobacterial killing by rat macrophages through a nitric oxide-dependent
753 pathway. *Am J Physiol Lung Cell Mol Physiol* 279, L216.
- 754 Weikert, L.F., Edwards, K., Chroneos, Z.C., Hager, C., Hoffman, L., Shepherd, V.L. 1997. SP-A
755 enhances uptake of bacillus Calmette-Guerin by macrophages through a specific SP-A
756 receptor. *Am J Physiol* 272, L989.
- 757 Minutti, C.M., Jackson-Jones, L.H., Garcia-Fojeda, B., Knipper, J.A., Sutherland, T.E., Logan, N.,
758 Rinqvist, E., Guillamat-Prats, R., Ferenbach, D.A., Artigas, A., Stamme, C., Chroneos, Z.C.,
759 Zaiss, D.M., Casals, C., Allen, J.E. 2017. Local amplifiers of IL-4Ralpha-mediated macrophage
760 activation promote repair in lung and liver. *Science* 356, 1076.
- 761 Mori, K., Furusawa, T., Okubo, T., Inoue, T., Ikawa, S., Yanai, N., Mori, K.J., Obinata, M. 2003.
762 Genome structure and differential expression of two isoforms of a novel PDZ-containing
763 myosin (MysPDZ) (Myo18A). *J Biochem* 133, 405.
- 764 Yang, C.H., Szeliga, J., Jordan, J., Faske, S., Sever-Chroneos, Z., Dorsett, B., Christian, R.E., Settlege,
765 R.E., Shabanowitz, J., Hunt, D.F., Whitsett, J.A., Chroneos, Z.C. 2005. Identification of the
766 surfactant protein A receptor 210 as the unconventional myosin 18A. *J Biol Chem* 280, 34447.
- 767 Szeliga, J., Jordan, J., Yang, C.H., Sever-Chroneos, Z., Chroneos, Z.C. 2005. Bacterial expression of
768 recombinant MyoXVIIIa domains. *Anal Biochem* 346, 179.
- 769 Taft, M.H., Latham, S.L. 2020. Myosin XVIII. *Adv Exp Med Biol* 1239, 421.

- 770 Lee, I.C., Leung, T., Tan, I. 2014. Adaptor protein LRAP25 mediates myotonic dystrophy kinase-
771 related Cdc42-binding kinase (MRCK) regulation of LIMK1 protein in lamellipodial F-actin
772 dynamics. *J Biol Chem* 289, 26989.
- 773 Ng, M.M., Dippold, H.C., Buschman, M.D., Noakes, C.J., Field, S.J. 2013. GOLPH3L antagonizes
774 GOLPH3 to determine Golgi morphology. *Mol Biol Cell* 24, 796.
- 775 Horsthemke, M., Nutter, L.M.J., Bachg, A.C., Skryabin, B.V., Honnert, U., Zobel, T., Bogdan, S., Stoll,
776 M., Seidl, M.D., Muller, F.U., Ravens, U., Unger, A., Linke, W.A., van Gorp, P.R.R., de Vries,
777 A.A.F., Bahler, M., Hanley, P.J. 2019. A novel isoform of myosin 18A (Myo18A γ) is an
778 essential sarcomeric protein in mouse heart. *J Biol Chem* 294, 7202.
- 779 Cross, M., Csar, X.F., Wilson, N.J., Manes, G., Addona, T.A., Marks, D.C., Whitty, G.A., Ashman, K.,
780 Hamilton, J.A. 2004. A novel 110 kDa form of myosin XVIIIa (MysPDZ) is tyrosine-
781 phosphorylated after colony-stimulating factor-1 receptor signalling. *Biochem J* 380, 243.
- 782 De Masson, A., Giustiniani, J., Marie-Cardine, A., Bouaziz, J.D., Dulphy, N., Gossot, D., Validire, P.,
783 Tazi, A., Garbar, C., Bagot, M., Merrouche, Y., Bensussan, A. 2016. Identification of CD245 as
784 myosin 18A, a receptor for surfactant A: A novel pathway for activating human NK
785 lymphocytes. *Oncoimmunology* 5, e1127493.
- 786 Samten, B., Townsend, J.C., Sever-Chroneos, Z., Pasquinelli, V., Barnes, P.F., Chroneos, Z.C. 2008. An
787 antibody against the surfactant protein A (SP-A)-binding domain of the SP-A receptor inhibits
788 T cell-mediated immune responses to *Mycobacterium tuberculosis*. *J Leukoc Biol* 84, 115.
- 789 Chroneos, Z., Shepherd, V.L. 1995. Differential regulation of the mannose and SP-A receptors on
790 macrophages. *Am J Physiol* 269, L721.
- 791 Jean Beltran, P.M., Mathias, R.A., Cristea, I.M. 2016. A Portrait of the Human Organelle Proteome In
792 Space and Time during Cytomegalovirus Infection. *Cell Syst* 3, 361.
- 793 Sever-Chroneos, Z., Krupa, A., Davis, J., Hasan, M., Yang, C.H., Szeliga, J., Herrmann, M., Hussain, M.,
794 Geisbrecht, B.V., Kobzik, L., Chroneos, Z.C. 2011. Surfactant protein A (SP-A)-mediated
795 clearance of *Staphylococcus aureus* involves binding of SP-A to the staphylococcal adhesin
796 eap and the macrophage receptors SP-A receptor 210 and scavenger receptor class A. *J Biol*
797 *Chem* 286, 4854.
- 798 Borron, P., McCormack, F.X., Elhalwagi, B.M., Chroneos, Z.C., Lewis, J.F., Zhu, S., Wright, J.R.,
799 Shepherd, V.L., Possmayer, F., Inchley, K., Fraher, L.J. 1998. Surfactant protein A inhibits T
800 cell proliferation via its collagen-like tail and a 210-kDa receptor. *Am J Physiol* 275, L679.
- 801 Chroneos, Z.C., Abdolrasulnia, R., Whitsett, J.A., Rice, W.R., Shepherd, V.L. 1996. Purification of a
802 cell-surface receptor for surfactant protein A. *J Biol Chem* 271, 16375.
- 803 Lopez-Sanchez, A., Saenz, A., Casals, C. 2010. Surfactant protein A (SP-A)-tacrolimus complexes have
804 a greater anti-inflammatory effect than either SP-A or tacrolimus alone on human
805 macrophage-like U937 cells. *European journal of pharmaceuticals and biopharmaceutics :*
806 *official journal of Arbeitsgemeinschaft fur Pharmazeutische Verfahrenstechnik e.V.*
- 807 Stamme, C., Walsh, E., Wright, J.R. 2000. Surfactant protein A differentially regulates IFN- γ -
808 and LPS-induced nitrite production by rat alveolar macrophages. *Am J Respir Cell Mol Biol* 23,
809 772.
- 810 Sever-Chroneos, Z., Murthy, A., Davis, J., Florence, J.M., Kurdowska, A., Krupa, A., Tichelaar, J.W.,
811 White, M.R., Hartshorn, K.L., Kobzik, L., Whitsett, J.A., Chroneos, Z.C. 2011. GM-CSF
812 modulates pulmonary resistance to influenza A infection. *Antiviral Res* 92, 319.
- 813 Fino, K.K., Yang, L., Silveyra, P., Hu, S., Umstead, T.M., DiAngelo, S., Halstead, E.S., Cooper, T.K.,
814 Abraham, T., Takahashi, Y., Zhou, Z., Wang, H.G., Chroneos, Z.C. 2017. SH3GLB2/endophilin

- 815 B2 regulates lung homeostasis and recovery from severe influenza A virus infection. *Sci Rep*
816 7, 7262.
- 817 Kim, D., Langmead, B., Salzberg, S.L. 2015. HISAT: a fast spliced aligner with low memory
818 requirements. *Nat Methods* 12, 357.
- 819 Liao, Y., Smyth, G.K., Shi, W. 2019. The R package Rsubread is easier, faster, cheaper and better for
820 alignment and quantification of RNA sequencing reads. *Nucleic Acids Res* 47, e47.
- 821 Love, M.I., Huber, W., Anders, S. 2014. Moderated estimation of fold change and dispersion for
822 RNA-seq data with DESeq2. *Genome Biol* 15, 550.
- 823 Kanehisa, M., Goto, S. 2000. KEGG: kyoto encyclopedia of genes and genomes. *Nucleic Acids Res* 28,
824 27.
- 825 Korotkevich, G., Sukhov, V., Sergushichev, A. 2019. Fast gene set enrichment analysis. *bioRxiv*,
826 060012.
- 827 Wang, H., Song, C., Ding, Y., Pan, X., Ge, Z., Tan, B.H., Gowda, C., Sachdev, M., Muthusami, S.,
828 Ouyang, H., Lai, L., Francis, O.L., Morris, C.L., Abdel-Azim, H., Dorsam, G., Xiang, M., Payne,
829 K.J., Dovat, S. 2016. Transcriptional Regulation of JARID1B/KDM5B Histone Demethylase by
830 Ikaros, Histone Deacetylase 1 (HDAC1), and Casein Kinase 2 (CK2) in B-cell Acute
831 Lymphoblastic Leukemia. *J Biol Chem* 291, 4004.
- 832 Zhu, L.J., Gazin, C., Lawson, N.D., Pages, H., Lin, S.M., Lapointe, D.S., Green, M.R. 2010.
833 ChIPpeakAnno: a Bioconductor package to annotate ChIP-seq and ChIP-chip data. *BMC*
834 *Bioinformatics* 11, 237.
- 835 Yu, G., Wang, L.G., He, Q.Y. 2015. ChIPseeker: an R/Bioconductor package for ChIP peak annotation,
836 comparison and visualization. *Bioinformatics* 31, 2382.
- 837 Yu, G., He, Q.Y. 2016. ReactomePA: an R/Bioconductor package for reactome pathway analysis and
838 visualization. *Mol Biosyst* 12, 477.
- 839 Glass, C.K., Natoli, G. 2016. Molecular control of activation and priming in macrophages. *Nat*
840 *Immunol* 17, 26.
- 841 Hoogenkamp, M., Kryszynska, H., Ingram, R., Huang, G., Barlow, R., Clarke, D., Ebraldze, A., Zhang, P.,
842 Tagoh, H., Cockerill, P.N., Tenen, D.G., Bonifer, C. 2007. The Pu.1 locus is differentially
843 regulated at the level of chromatin structure and noncoding transcription by alternate
844 mechanisms at distinct developmental stages of hematopoiesis. *Mol Cell Biol* 27, 7425.
- 845 Imperato, M.R., Cauchy, P., Obier, N., Bonifer, C. 2015. The RUNX1-PU.1 axis in the control of
846 hematopoiesis. *Int J Hematol* 101, 319.
- 847 Petrovick, M.S., Hiebert, S.W., Friedman, A.D., Hetherington, C.J., Tenen, D.G., Zhang, D.E. 1998.
848 Multiple functional domains of AML1: PU.1 and C/EBPalpha synergize with different regions
849 of AML1. *Mol Cell Biol* 18, 3915.
- 850 Schmidt, S.V., Krebs, W., Ulas, T., Xue, J., Bassler, K., Gunther, P., Hardt, A.L., Schultze, H., Sander, J.,
851 Klee, K., Theis, H., Kraut, M., Beyer, M., Schultze, J.L. 2016. The transcriptional regulator
852 network of human inflammatory macrophages is defined by open chromatin. *Cell Res* 26,
853 151.
- 854 Berclaz, P.Y., Carey, B., Fillipi, M.D., Wernke-Dollries, K., Geraci, N., Cush, S., Richardson, T.,
855 Kitzmiller, J., O'Connor, M., Hermoyan, C., Korfhagen, T., Whitsett, J.A., Trapnell, B.C. 2007.
856 GM-CSF regulates a PU.1-dependent transcriptional program determining the pulmonary
857 response to LPS. *American journal of respiratory cell and molecular biology* 36, 114.
- 858 Cheng, J.X., Anastasi, J., Watanabe, K., Kleinbrink, E.L., Grimley, E., Knibbs, R., Shen, Q.J., Vardiman,
859 J.W. 2013. Genome-wide profiling reveals epigenetic inactivation of the PU.1 pathway by

- 860 histone H3 lysine 27 trimethylation in cytogenetically normal myelodysplastic syndrome.
861 Leukemia 27, 1291.
- 862 Burda, P., Vargova, J., Curik, N., Salek, C., Papadopoulos, G.L., Strouboulis, J., Stopka, T. 2016. GATA-
863 1 Inhibits PU.1 Gene via DNA and Histone H3K9 Methylation of Its Distal Enhancer in
864 Erythroleukemia. PLoS One 11, e0152234.
- 865 Tagore, M., McAndrew, M.J., Gjidoda, A., Floer, M. 2015. The Lineage-Specific Transcription Factor
866 PU.1 Prevents Polycomb-Mediated Heterochromatin Formation at Macrophage-Specific
867 Genes. Mol Cell Biol 35, 2610.
- 868 K, D., VR, P., P, R., X, X., P, B. 2011. MotifMap: integrative genome-wide maps of regulatory motif
869 sites for model species. BMC bioinformatics 12.
- 870 G, M., S, S., AJ, T., J, T., SJ, M., M, W., Y, G., C, F., J, B., G, K., C, P., V, O., S, T., DG, T., C, P., T, E. 2013.
871 Dynamic analysis of gene expression and genome-wide transcription factor binding during
872 lineage specification of multipotent progenitors. Cell stem cell 13.
- 873 V, B. 2016. Analysis of Genomic Sequence Motifs for Deciphering Transcription Factor Binding and
874 Transcriptional Regulation in Eukaryotic Cells. Frontiers in genetics 7.
- 875 Carey, B., Staudt, M.K., Bonaminio, D., van der Loo, J.C., Trapnell, B.C. 2007. PU.1 redirects
876 adenovirus to lysosomes in alveolar macrophages, uncoupling internalization from infection.
877 Journal of immunology 178, 2440.
- 878 Umstead, T.M., Hewage, E.K., Mathewson, M., Beaudoin, S., Chroneos, Z.C., Wang, M., Halstead, E.S.
879 2020. Lower respiratory tract delivery, airway clearance, and preclinical efficacy of inhaled
880 GM-CSF in a postinfluenza pneumococcal pneumonia model. Am J Physiol Lung Cell Mol
881 Physiol 318, L571.
- 882 Huang, F.F., Barnes, P.F., Feng, Y., Donis, R., Chroneos, Z.C., Idell, S., Allen, T., Perez, D.R., Whitsett,
883 J.A., Dunussi-Joannopoulos, K., Shams, H. 2011. GM-CSF in the lung protects against lethal
884 influenza infection. Am J Respir Crit Care Med 184, 259.
- 885 Marvin, S.A., Russier, M., Huerta, C.T., Russell, C.J., Schultz-Cherry, S. 2017. Influenza Virus
886 Overcomes Cellular Blocks To Productively Replicate, Impacting Macrophage Function. J
887 Virol 91.
- 888 Cline, T.D., Beck, D., Bianchini, E. 2017. Influenza virus replication in macrophages: balancing
889 protection and pathogenesis. J Gen Virol 98, 2401.
- 890 Pradere, J.P., Hernandez, C., Koppe, C., Friedman, R.A., Luedde, T., Schwabe, R.F. 2016. Negative
891 regulation of NF-kappaB p65 activity by serine 536 phosphorylation. Sci Signal 9, ra85.
- 892 Song, Y.J., Jen, K.Y., Soni, V., Kieff, E., Cahir-McFarland, E. 2006. IL-1 receptor-associated kinase 1 is
893 critical for latent membrane protein 1-induced p65/RelA serine 536 phosphorylation and NF-
894 kappaB activation. Proc Natl Acad Sci U S A 103, 2689.
- 895 Schmeck, B., Zahlten, J., Moog, K., van Laak, V., Huber, S., Hocke, A.C., Opitz, B., Hoffmann, E.,
896 Kracht, M., Zerrahn, J., Hammerschmidt, S., Rosseau, S., Suttorp, N., Hippenstiel, S. 2004.
897 Streptococcus pneumoniae-induced p38 MAPK-dependent phosphorylation of RelA at the
898 interleukin-8 promoter. J Biol Chem 279, 53241.
- 899 Oishi, Y., Spann, N.J., Link, V.M., Muse, E.D., Strid, T., Edillor, C., Kolar, M.J., Matsuzaka, T.,
900 Hayakawa, S., Tao, J., Kaikkonen, M.U., Carlin, A.F., Lam, M.T., Manabe, I., Shimano, H.,
901 Saghatelian, A., Glass, C.K. 2017. SREBP1 Contributes to Resolution of Pro-inflammatory
902 TLR4 Signaling by Reprogramming Fatty Acid Metabolism. Cell Metab 25, 412.
- 903 Koundouros, N., Pouligiannis, G. 2020. Reprogramming of fatty acid metabolism in cancer. Br J
904 Cancer 122, 4.

- 905 Cucchi, D., Camacho-Munoz, D., Certo, M., Pucino, V., Nicolaou, A., Mauro, C. 2019. Fatty acids -
906 from energy substrates to key regulators of cell survival, proliferation and effector function.
907 *Cell Stress* 4, 9.
- 908 Spadaro, O., Camell, C.D., Bosurgi, L., Nguyen, K.Y., Youm, Y.H., Rothlin, C.V., Dixit, V.D. 2017. IGF1
909 Shapes Macrophage Activation in Response to Immunometabolic Challenge. *Cell Rep* 19, 225.
- 910 Kralova Lesna, I., Kralova, A., Cejkova, S., Fronek, J., Petras, M., Sekerkova, A., Thieme, F., Janousek,
911 L., Poledne, R. 2016. Characterisation and comparison of adipose tissue macrophages from
912 human subcutaneous, visceral and perivascular adipose tissue. *J Transl Med* 14, 208.
- 913 Cao, Q., Rong, S., Repa, J.J., St Clair, R., Parks, J.S., Mishra, N. 2014. Histone deacetylase 9 represses
914 cholesterol efflux and alternatively activated macrophages in atherosclerosis development.
915 *Arterioscler Thromb Vasc Biol* 34, 1871.
- 916 Li, X., Zhang, Q., Ding, Y., Liu, Y., Zhao, D., Zhao, K., Shen, Q., Liu, X., Zhu, X., Li, N., Cheng, Z., Fan, G.,
917 Wang, Q., Cao, X. 2016. Methyltransferase Dnmt3a upregulates HDAC9 to deacetylate the
918 kinase TBK1 for activation of antiviral innate immunity. *Nat Immunol* 17, 806.
- 919 Zhang, N., Sauve, A.A. 2018. Regulatory Effects of NAD(+) Metabolic Pathways on Sirtuin Activity.
920 *Prog Mol Biol Transl Sci* 154, 71.
- 921 Karpurapu, M., Wang, X., Deng, J., Park, H., Xiao, L., Sadikot, R.T., Frey, R.S., Maus, U.A., Park, G.Y.,
922 Scott, E.W., Christman, J.W. 2011. Functional PU.1 in macrophages has a pivotal role in NF-
923 kappaB activation and neutrophilic lung inflammation during endotoxemia. *Blood* 118, 5255.
- 924 Liu, J., Ma, X. 2006. Interferon regulatory factor 8 regulates RANTES gene transcription in
925 cooperation with interferon regulatory factor-1, NF-kappaB, and PU.1. *J Biol Chem* 281,
926 19188.
- 927 Rosa, A., Ballarino, M., Sorrentino, A., Sthandier, O., De Angelis, F.G., Marchioni, M., Masella, B.,
928 Guarini, A., Fatica, A., Peschle, C., Bozzoni, I. 2007. The interplay between the master
929 transcription factor PU.1 and miR-424 regulates human monocyte/macrophage
930 differentiation. *Proc Natl Acad Sci U S A* 104, 19849.
- 931 Celada, A., Borrás, F.E., Soler, C., Lloberas, J., Klemsz, M., van Beveren, C., McKercher, S., Maki, R.A.
932 1996. The transcription factor PU.1 is involved in macrophage proliferation. *J Exp Med* 184,
933 61.
- 934 Ha, S.D., Cho, W., DeKoter, R.P., Kim, S.O. 2019. The transcription factor PU.1 mediates enhancer-
935 promoter looping that is required for IL-1beta eRNA and mRNA transcription in mouse
936 melanoma and macrophage cell lines. *J Biol Chem* 294, 17487.
- 937 Qian, F., Deng, J., Lee, Y.G., Zhu, J., Karpurapu, M., Chung, S., Zheng, J.N., Xiao, L., Park, G.Y.,
938 Christman, J.W. 2015. The transcription factor PU.1 promotes alternative macrophage
939 polarization and asthmatic airway inflammation. *J Mol Cell Biol* 7, 557.
- 940 Rothenberg, E.V., Hosokawa, H., Ungerback, J. 2019. Mechanisms of Action of Hematopoietic
941 Transcription Factor PU.1 in Initiation of T-Cell Development. *Front Immunol* 10, 228.
- 942 Ghisletti, S., Barozzi, I., Mietton, F., Polletti, S., De Santa, F., Venturini, E., Gregory, L., Lonie, L., Chew,
943 A., Wei, C.L., Ragoussis, J., Natoli, G. 2010. Identification and characterization of enhancers
944 controlling the inflammatory gene expression program in macrophages. *Immunity* 32, 317.
- 945 van Riel, B., Rosenbauer, F. 2014. Epigenetic control of hematopoiesis: the PU.1 chromatin
946 connection. *Biol Chem* 395, 1265.
- 947 Leddin, M., Perrod, C., Hoogenkamp, M., Ghani, S., Assi, S., Heinz, S., Wilson, N.K., Follows, G.,
948 Schonheit, J., Vockentanz, L., Mosammam, A.M., Chen, W., Tenen, D.G., Westhead, D.R.,
949 Gottgens, B., Bonifer, C., Rosenbauer, F. 2011. Two distinct auto-regulatory loops operate at
950 the PU.1 locus in B cells and myeloid cells. *Blood* 117, 2827.

951 Minderjahn, J., Schmidt, A., Fuchs, A., Schill, R., Raithel, J., Babina, M., Schmidl, C., Gebhard, C.,
952 Schmidhofer, S., Mendes, K., Ratermann, A., Glatz, D., Nutzel, M., Edinger, M., Hoffmann, P.,
953 Spang, R., Langst, G., Imhof, A., Rehli, M. 2020. Mechanisms governing the pioneering and
954 redistribution capabilities of the non-classical pioneer PU.1. *Nat Commun* 11, 402.
955 McAndrew, M.J., Gjidoda, A., Tagore, M., Miksanek, T., Floer, M. 2016. Chromatin Remodeler
956 Recruitment during Macrophage Differentiation Facilitates Transcription Factor Binding to
957 Enhancers in Mature Cells. *J Biol Chem* 291, 18058.
958 Blau, H., Riklis, S., Kravtsov, V., Kalina, M. 1994. Secretion of cytokines by rat alveolar epithelial cells:
959 possible regulatory role for SP-A. *Am J Physiol* 266, L148.
960 Yoshida, M., Ikegami, M., Reed, J.A., Chroneos, Z.C., Whitsett, J.A. 2001. GM-CSF regulates protein
961 and lipid catabolism by alveolar macrophages. *Am J Physiol Lung Cell Mol Physiol* 280, L379.
962

963 12 Figures

964 **Figure 1. Differentially Expressed genes are associated with upregulation of Innate Immune**
965 **Sensing Pathways. (a)** Cells were cultured overnight a 2E5 cells/well and removed using Cell
966 Dissociation Media. Cells were washed, blocked with BD Mouse Fc Block, and stained with
967 fluorescent antibodies against specific cell surface markers. Stained cells were analyzed using a LSR
968 II flow cytometer with compensation and gating analysis performed on FlowJo v 9.9.5. Data plotted
969 is mean of mean fluorescence intensity \pm S.E. (n=3), **, adjusted p-value <0.005 compared to WT;
970 ***, adjusted p-value <0.0005 compared to WT. **(b, c)** RNA isolated from WT and SP-R210_L(DN) cells
971 cultured overnight was sequenced and aligned to the mm10 database using hisat2 with read counts
972 obtained using featurecounts. Count data was then compared between genotypes with three
973 replicates per cell type using deseq2. Differently expressed genes between SP-R210_L(DN) and WT
974 cells **(b)** were filtered by p-value <0.05. These gene sets were then filtered using the MGI Immune
975 Genes database to elucidate differentially expressed immune genes **(c)** – SP-R210_L(DN) vs WT) The
976 genes were also labeled in red in **(b)**. Differentially expressed RNA genes were mapped to KEGG
977 pathways using the fgsea R package. **(d)** Upregulated pathways were compared between SP-R210_L
978 and WT cells. Enrichment plots for Cytosolic DNA Sensing Pathway and TLR Signaling Pathway were
979 included to show enrichment in genes associated with these gene sets. **(e)** The enrichment scores
980 for the 10 disease associated pathways with the lowest p-values were plotted for SP-R210_L(DN) vs
981 WT cells.

982 **Figure 2. PU.1 binding across the genome is altered with SP-R210_L depletion.** ChIP was used to
983 precipitate PU.1-bound genomic regions, then sequenced and aligned to the mm10 genome.

984 Concordant peaks between two experimental replicates determined using overlapping peaks
985 function of ChIPPeakAnno were used for further analysis. **(a)** Peaks between WT and SP-R210_L(DN)
986 cells were compared using ChIPPeakAnno to identify the concordance in peaks between the two
987 genotypes, showing 6140 peaks consistent with both genotypes, and 5365 peaks unique to SP-
988 R210_L(DN) cells. The peak distribution across genome was increased in SP-R210_L(DN) cells **(a)**. **(b)**
989 Using Chipseeker, the identified peaks were associated with genomic features for WT and SP-
990 R210_L(DN) cells showed decrease PU.1 binding in promoter regions, but with slightly increased
991 binding in 3' UTR, Exon, and Intron regions. **(c)** Association between unique ChIP peaks in each cell
992 type and RNA expression. Of the 5365 PU.1 peaks unique to SP-R210_L(DN) cells, 437 peaks were
993 associated with RNA transcripts upregulated in WT cells, while 573 peaks were associated with RNA
994 transcripts upregulated in SP-R210_L(DN) cells. Of 1011 PU.1 peaks unique to WT cells, 260 peaks
995 were associated with genes with upregulated RNA transcripts in WT cells, and 49 peaks associated
996 with upregulated in SP-R210_L(DN) cells. **(d)** PU.1 associated genes were mapped to Reactome
997 pathways using ReactomePA. Pathway enrichment scores and p-values for WT and SP-R210_L(DN)
998 cells were plotted in a heat map; each pathway was associated to larger Reactome pathway families.
999

1000 **Figure 3. SP-R210_L(DN) cells have altered histone methylation. (a)** ChIP-seq of H3K4me3 was
1001 performed for both WT and SP-R210_L(DN) cells, showing increased H3K4me3 marks in SP-R210_L(DN)
1002 cells. **(b)** Genomic features associated with H3K4me3 marks were analyzed for both cell types,
1003 showing decreased H3K4me3 marks in promoter regions, but increased in intron and intergenic
1004 regions. This analysis was repeated for H3K9me3 **(c, d)** and H3K27me3 **(e, f)** methylation marks. For
1005 both H3K9me3 and H3K27me3, there were decreased amounts of these marks in SP-R210_L(DN) cells,
1006 with similar changes in genomic distribution; there were decreased H3K9me3 and H3K27me3 marks
1007 in promoter regions, but increased in Exon, Intron, and Intergenic regions. Using ChIPPeakAnno, it
1008 was seen that of the H3K4me marks, only a small proportion is associated with PU.1 peaks in both
1009 WT **(g)** and SP-R210_L(DN) **(h)** cells.

1010
1011 **Figure 4. PU.1 and H3K4me3 peaks Association with Genes are Altered with SP-R210_L(DN) cells. (a)**
1012 Bedgraphs were generated for PU.1 and H3K4me3 ChIP and mapped to UCSC mm10 annotated
1013 genome. Viewing TLR5 on the UCSC genome browser revealed increased PU.1 and H3K4me3
1014 binding at the promoter region of TLR5 in SP-R210_L(DN) cells. Additional bedgraphs of TLR genes can

1015 be found in Supplemental Figure 5, Supplemental Figure 6. **(b)** PU.1 is known to bind its own
1016 enhancer region; visualizing PU.1 on the genome browser revealed PU.1 binding sites in the
1017 enhancer region of PU.1 in both WT and SP-R210_L(DN) cells. **(c)** Investigating the Myo18A gene
1018 revealed several PU.1 peaks in both WT and SP-R210_L(DN) cells of varying intensities. H3K4me3
1019 peaks were found at the promoter region of Myo18a, as well as an internal start site. Highlighted in
1020 light blue is a predicted PU.1 binding site (UCI Motifmap), with the sequence depicted below. The
1021 sequence of a PU.1 peak present internal to Myo18A is also depicted. Within the sequence, a
1022 canonical PU.1 binding motif is highlighted in dark green.

1023

1024 **Figure 5. IAV infection affects PU.1 binding differently in SP-R210_L(DN) cells than WT cells. (a)**
1025 PU.1 peaks were compared between uninfected and infected WT and SP-R210_L(DN) cells to
1026 determine which peaks were similar or unique to each condition; infection reduces PU.1 binding in
1027 both WT and SP-R210_L(DN) cells. **(b)** IAV infection affects WT and SP-R210_L(DN) cells differently;
1028 while PU.1 binding with IAV infection has many shared regions with uninfected cells, some unique
1029 PU.1 bound regions in WT and SP-R210_L(DN) cells were identified with infection. IAV infected WT
1030 and SP-R210_L(DN) cells showed a majority of PU.1 bound regions to be similar, but each cell type
1031 also had numerous peaks that were unique with IAV infection. **(c)** PU.1 binding was mapped to
1032 genomic features for infected and uninfected WT and SP-R210_L(DN) cells. Mapping revealed
1033 increased distribution of PU.1 binding to promoter regions in WT and SP-R210_L(DN) cells, with
1034 concomitant decreases in Intron and Intergenic regions. **(d)** PU.1 associated regions were mapped
1035 to Reactome pathways; Pathway enrichment scores and p-values for WT and SP-R210_L(DN) cells
1036 were plotted in a heat map; each pathway was associated to larger Reactome pathway families.

1037

1038 **Figure 6. SP-R210_L knockdown alters phosphorylation of immune signaling molecules (a)** Clarified
1039 cell lysates from WT and SP-R210_L(DN) cells infected with PR8 for 3, 6, 12, and 24 hours were
1040 probed for phosphorylated and total IRF3 (a), IRF7 (b), NFκB p65 subunit (c, d) and P38 (e). **(a)** SP-
1041 R210_L(DN) cells show a trend towards increased baseline IRF3 phosphorylation, but less IRF3
1042 phosphorylation at 24 HPI (n=2). **(b)** SP-R210_L(DN) cells showed increased IRF7 phosphorylation at
1043 baseline, with significant increases at 12 and 24 HPI (n=3) **(c, d)** SP-R210_L(DN) cells showed
1044 increased Ser276 phosphorylation **(c)**, but decreased Ser536 **(d)**, of NFκB p65 compared with WT at
1045 baseline and throughout infection. (n=3) **(e)** WT cells exhibited increased phosphorylated P38 at 24

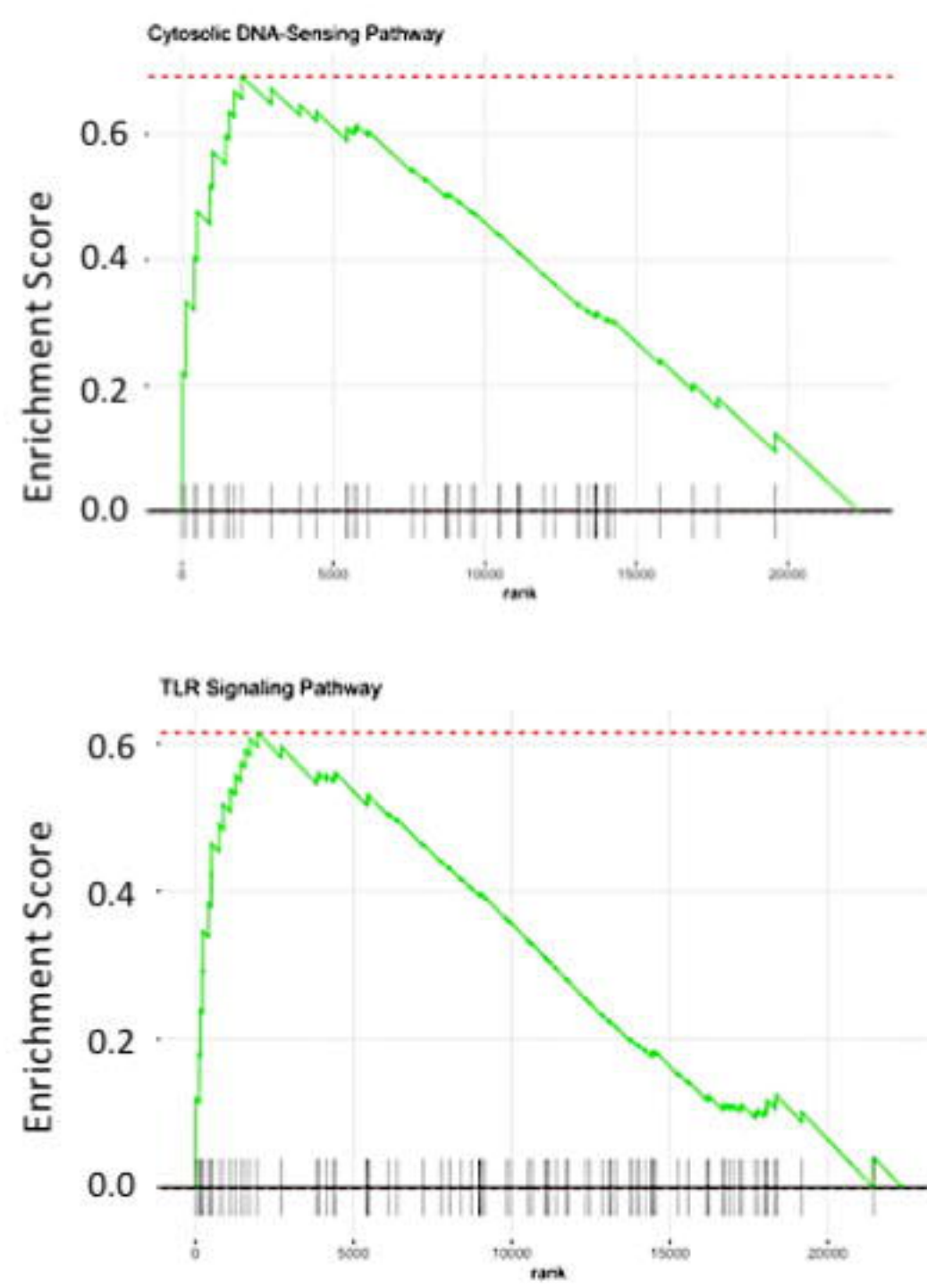
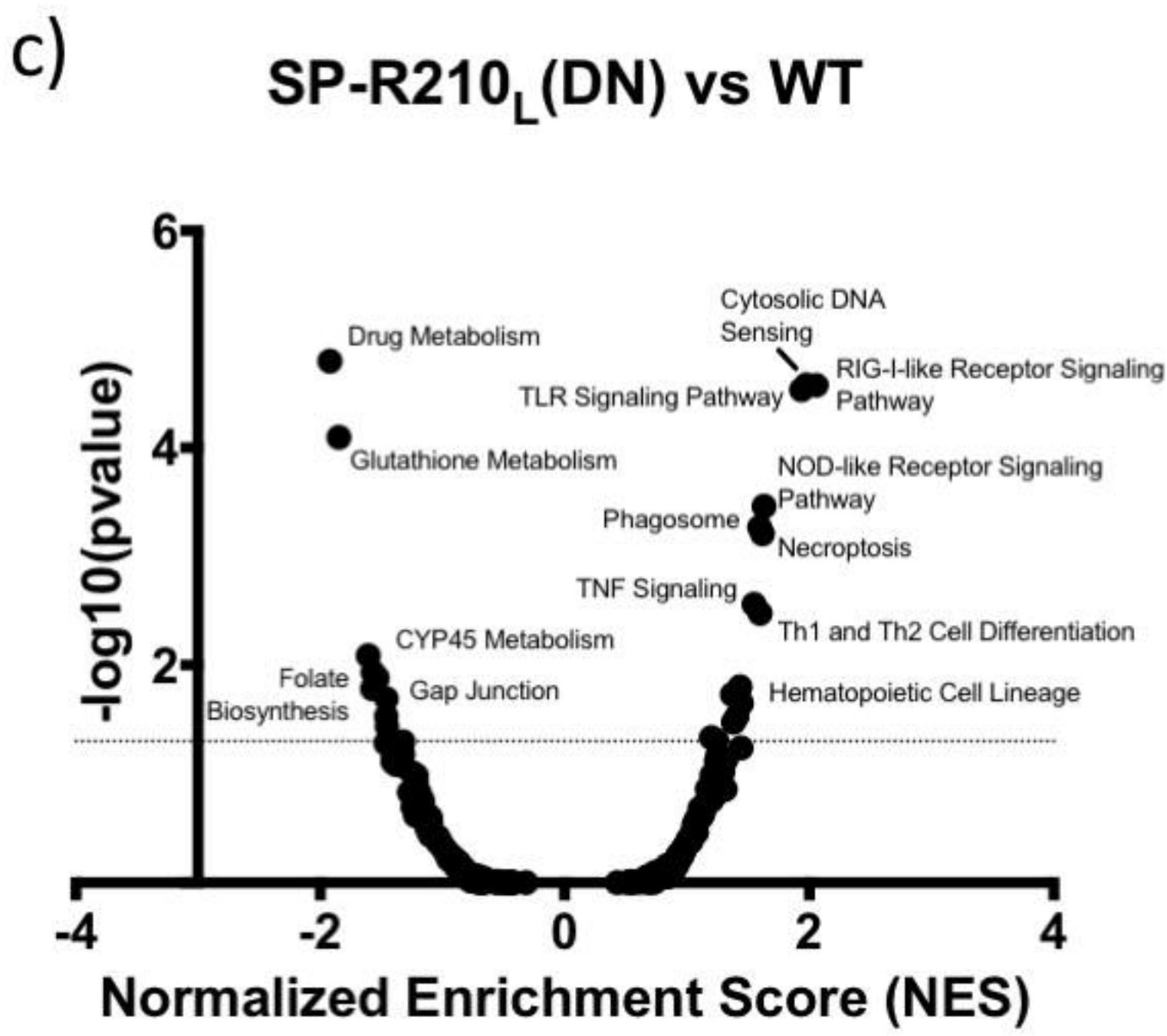
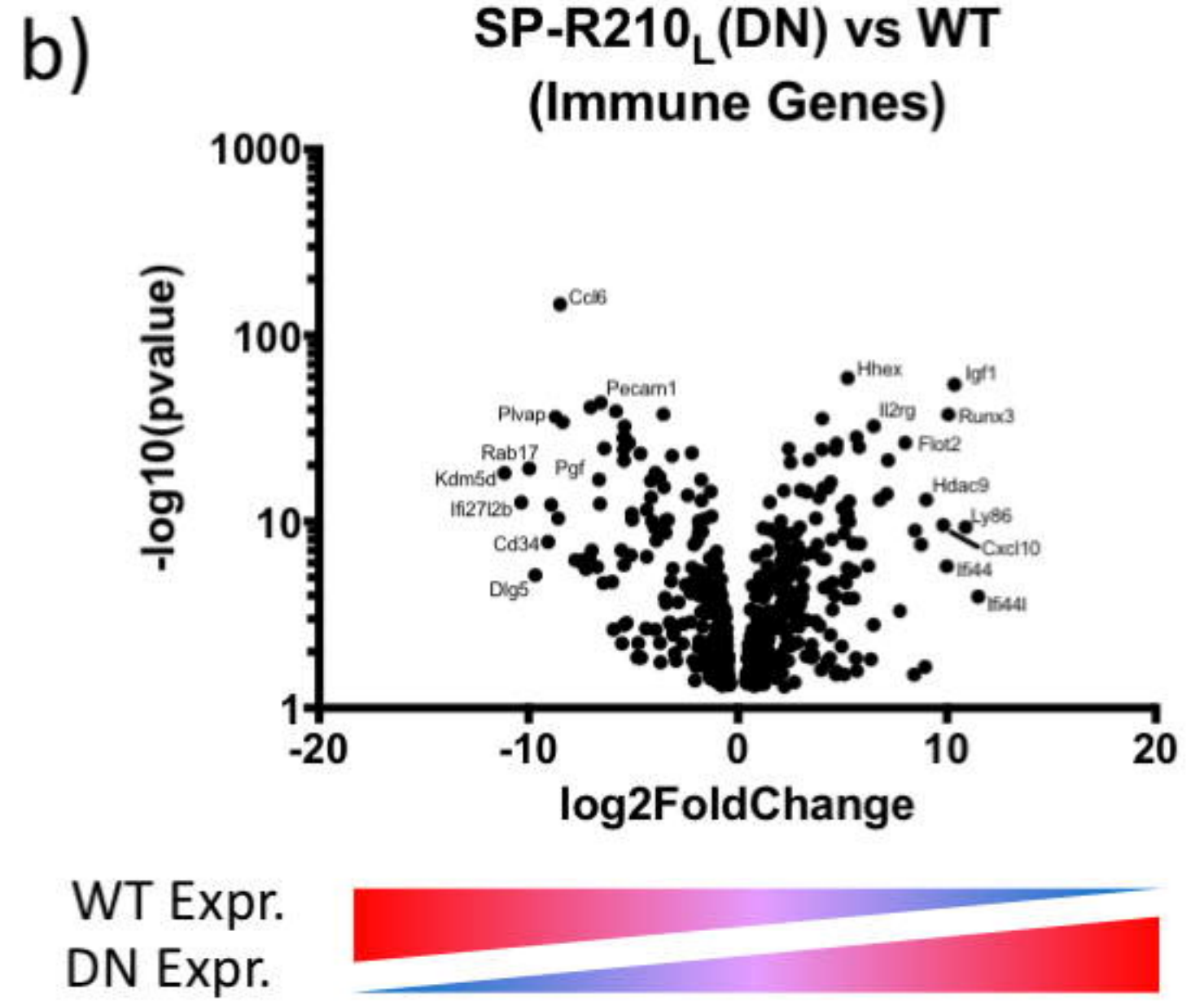
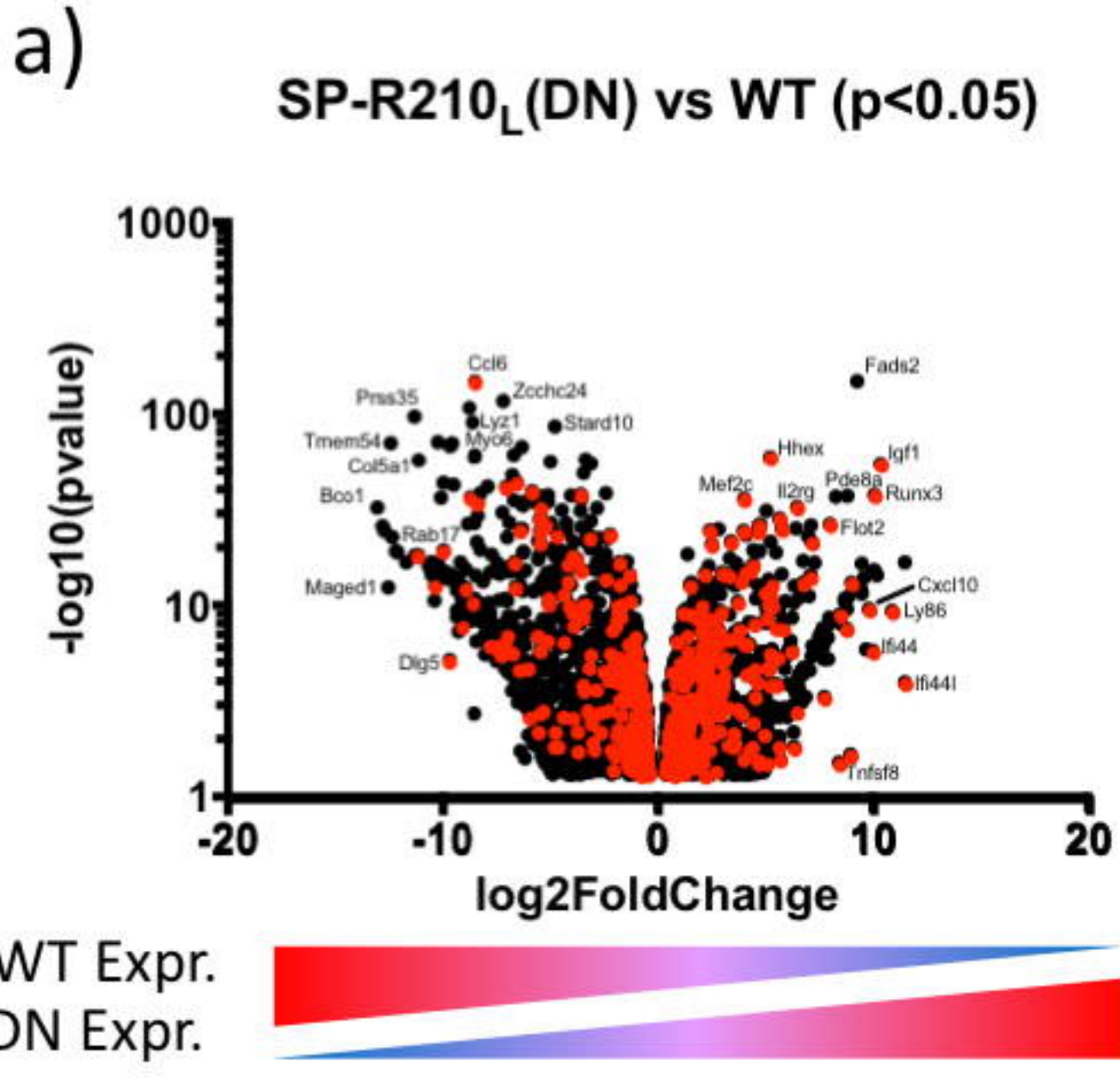
1046 hours post infection compared to SP-R210_L(DN) cells (n=3). Statistical significance determined by 2-
1047 way ANOVA. **, p-value <0.005 comparing between WT and SP-R210_L(DN); ***, p-value<0.005
1048 comparing between WT and SP-R210_L(DN); +, p-value <0.05 comparing between uninfected and
1049 infected time point; ++, p-value <0.005 comparing between uninfected and infected time point; +++,
1050 p-value <0.0005 comparing between uninfected and infected time point; +++, p-value <0.00005
1051 comparing between uninfected and infected time point

1052

1053 **13 Data Availability Statement**

1054 The datasets for this study can be found on GEO [].

Figure 1



d) **SP-R210_L(DN) vs WT Upregulated Disease-Associated Pathways**

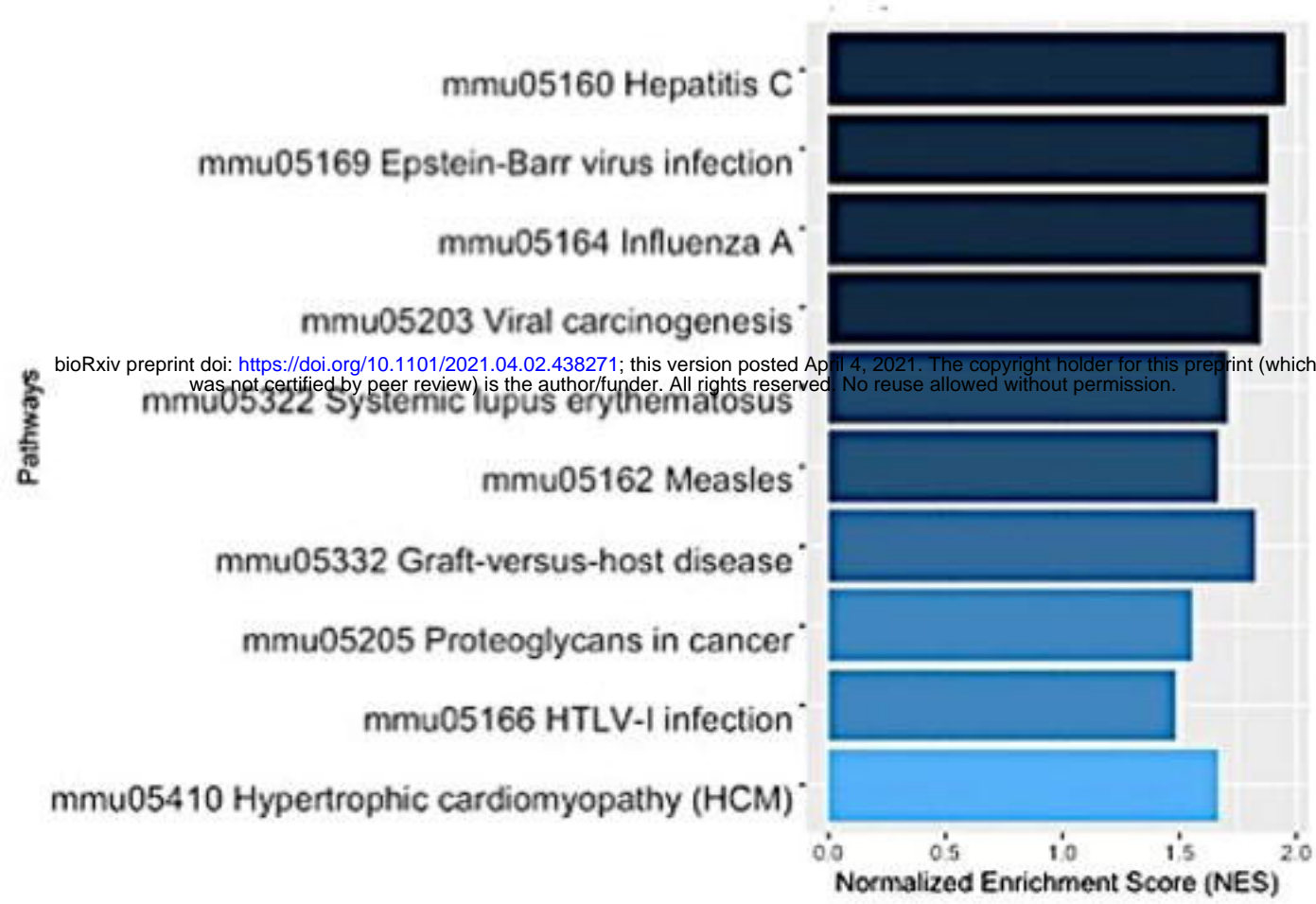
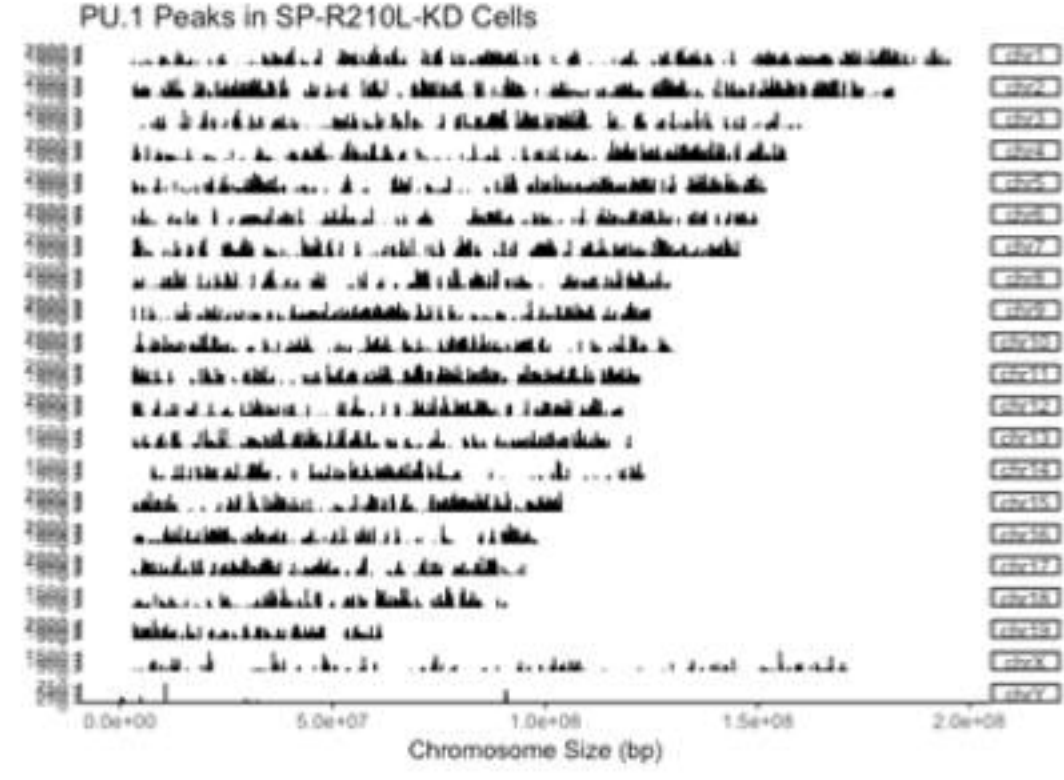
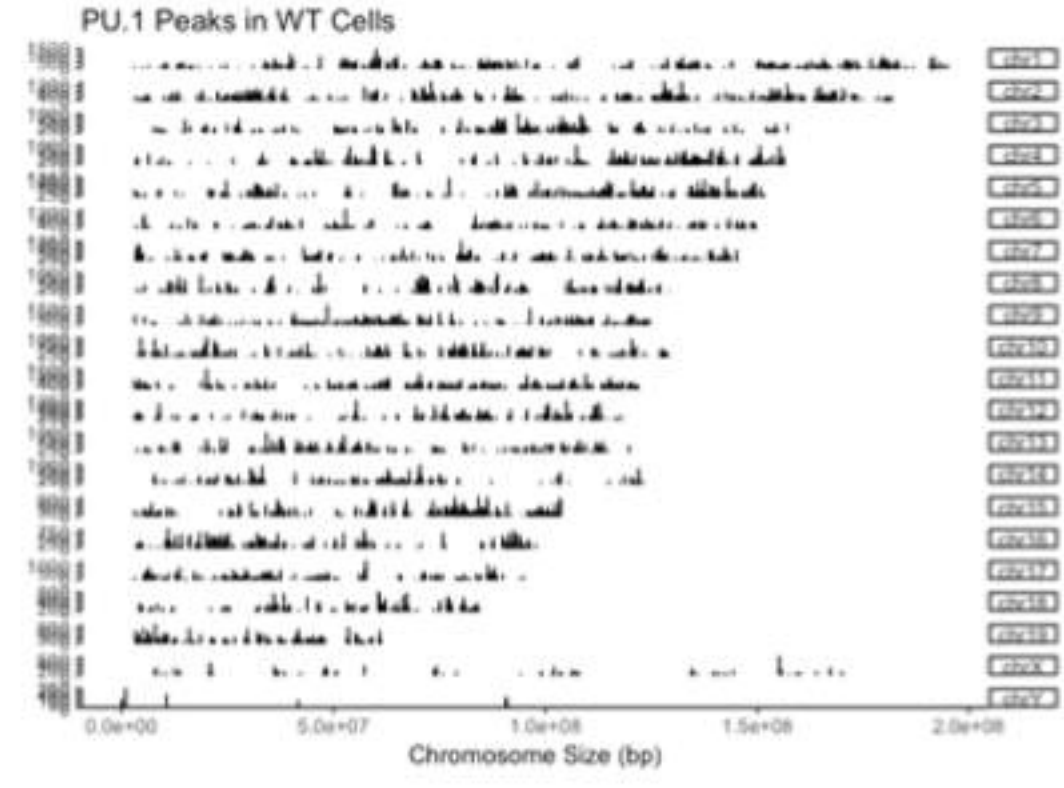
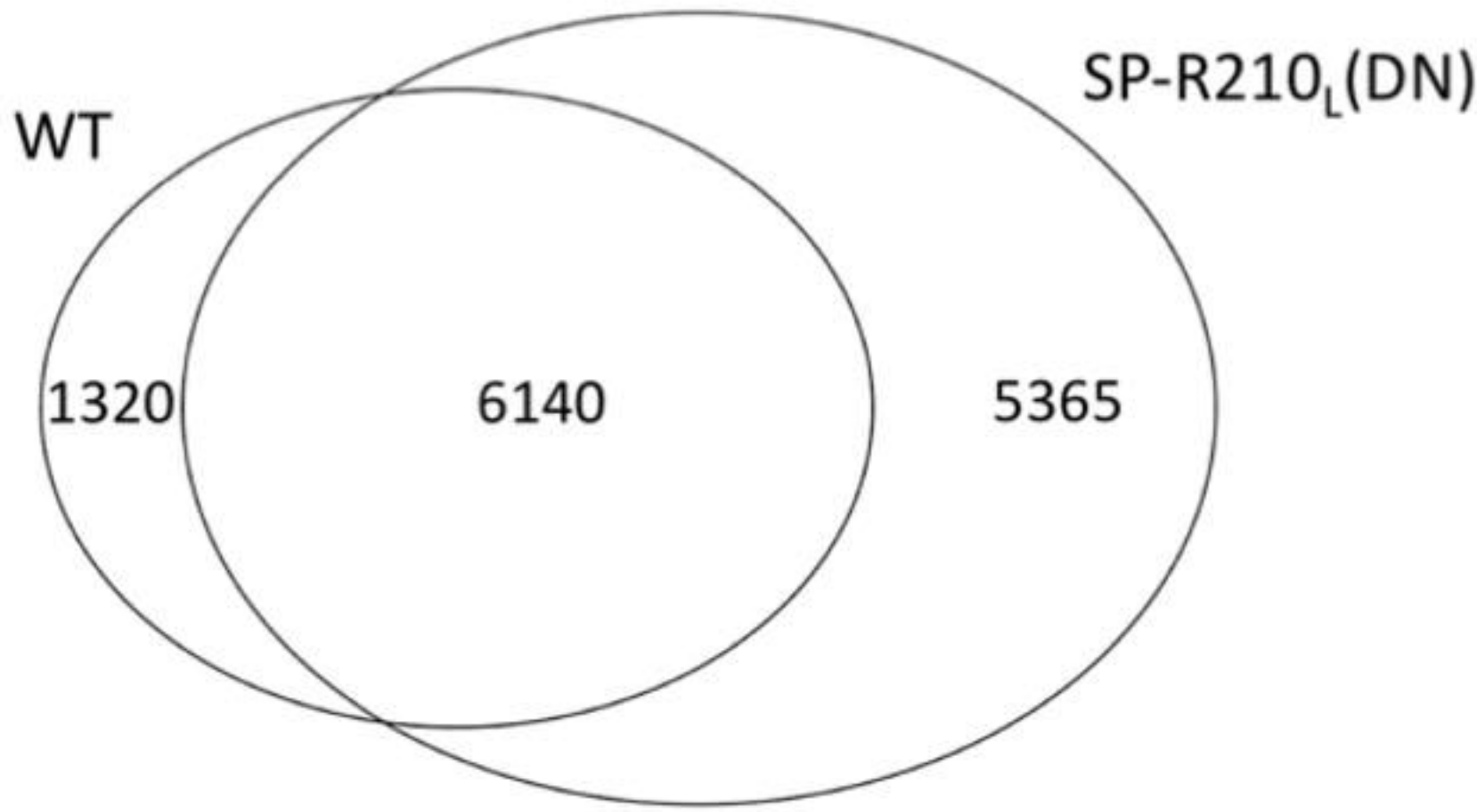


Figure 2

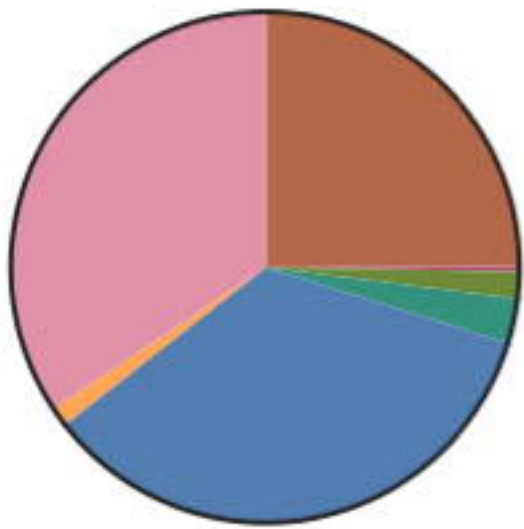
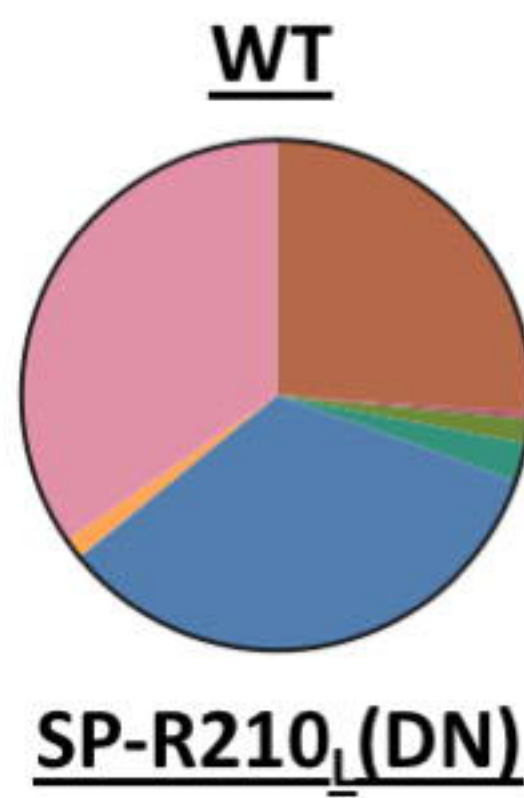
a)

**Peak Consensus:
WT vs SP-R210_L(DN) RAW 264.7 Cells**

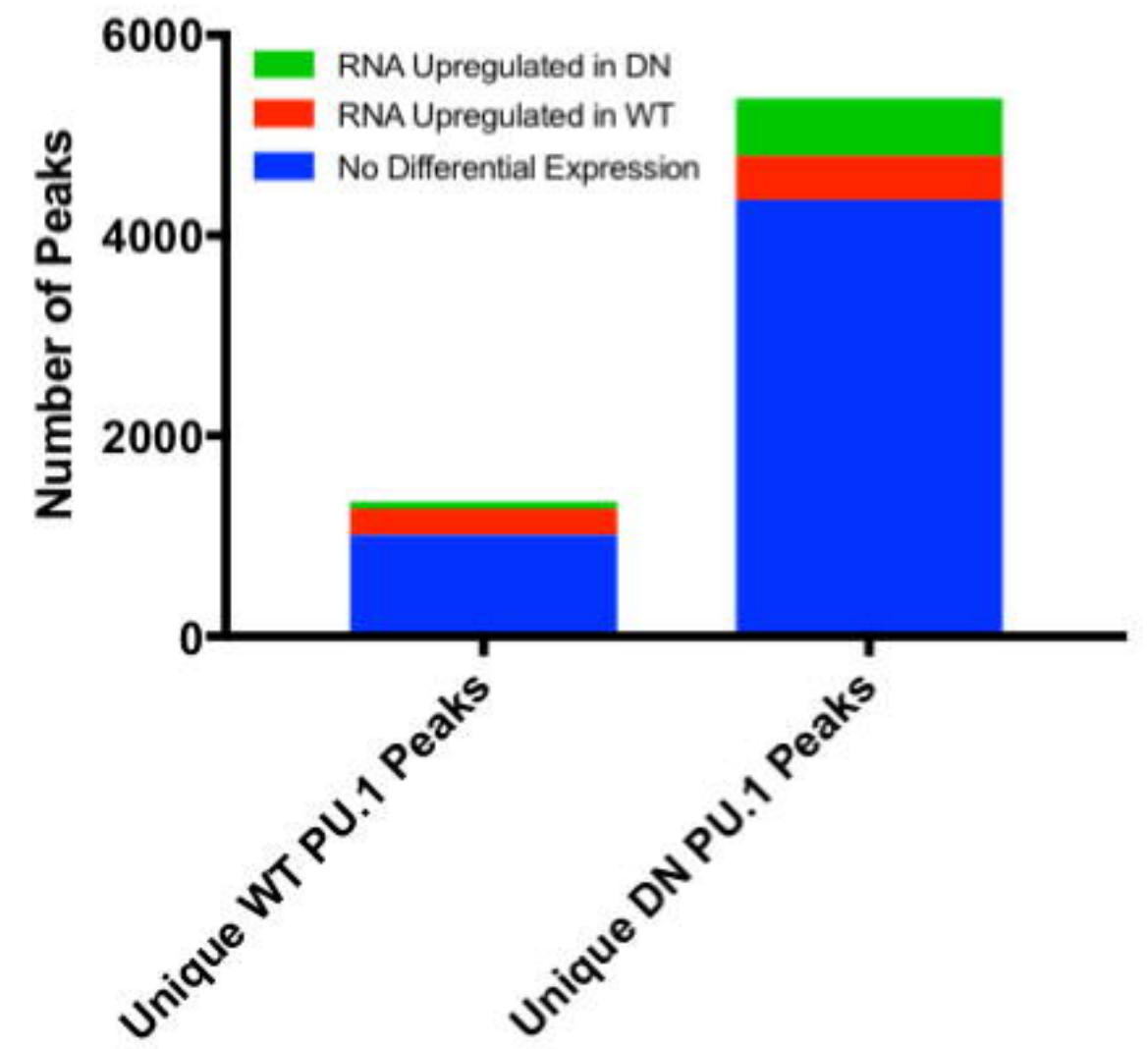


b)

	WT	SP-R210 _L (DN)
Promoter	26.11%	24.94%
Promoter (<=1 kb)	17.2%	16.06%
Promoter (1-2 kb)	4.9%	4.83%
Promoter (2-3 kb)	4.01%	4.05%
UTR regions	1.97%	2.03%
5' UTR	0.37%	0.34%
3' UTR	1.6%	1.69%
Exon Regions	2.4%	2.82%
1st Exon	0.36%	0.38%
Other Exon	2.04%	2.44%
Intron Regions	33.57%	34.64%
1st Intron	12.86%	12.84%
Other Intron	20.71%	21.8%
Downstream	1.31%	1.23%
Distal Intergenic	34.63%	34.34%



c)



d)

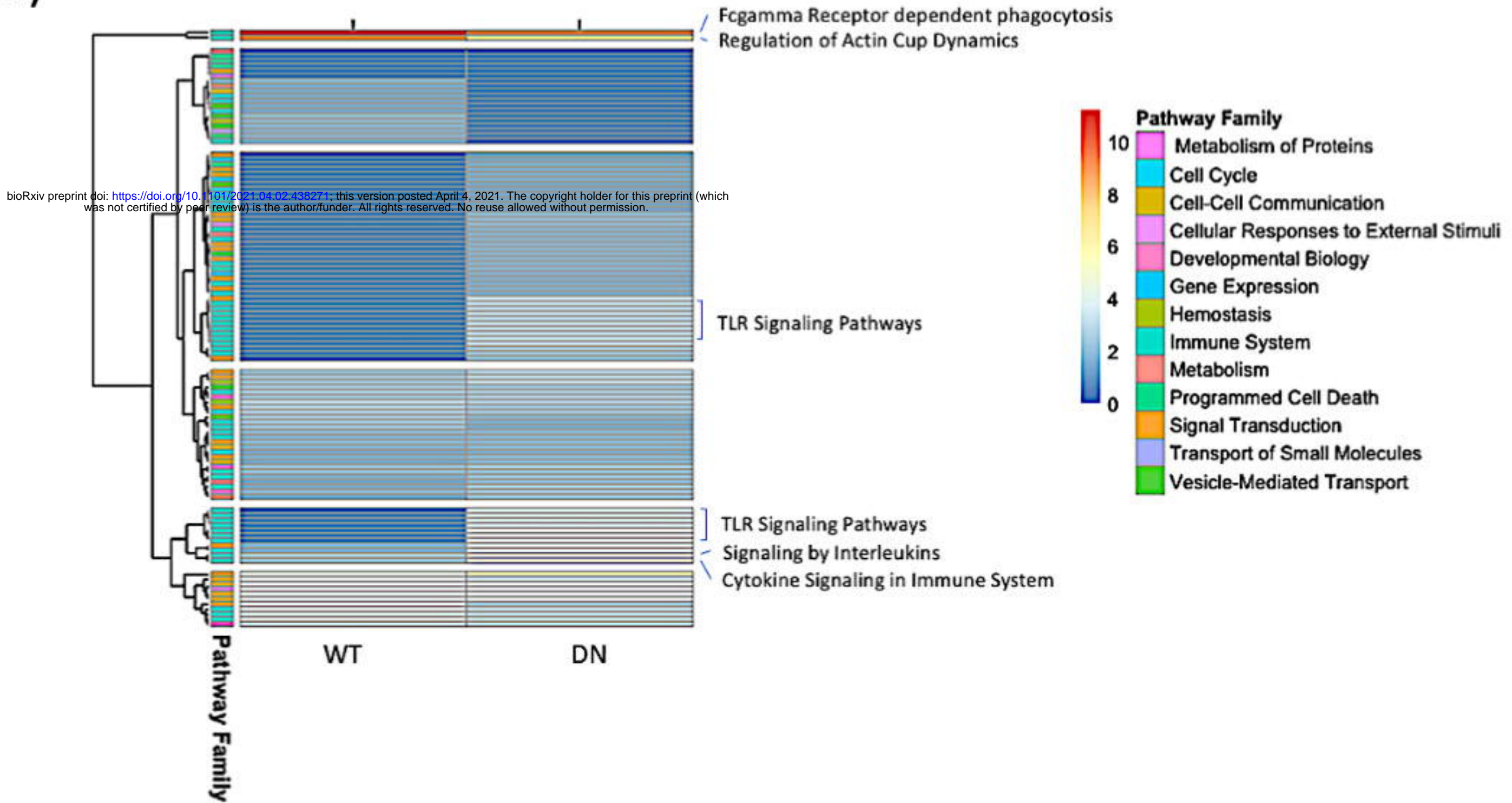


Figure 3

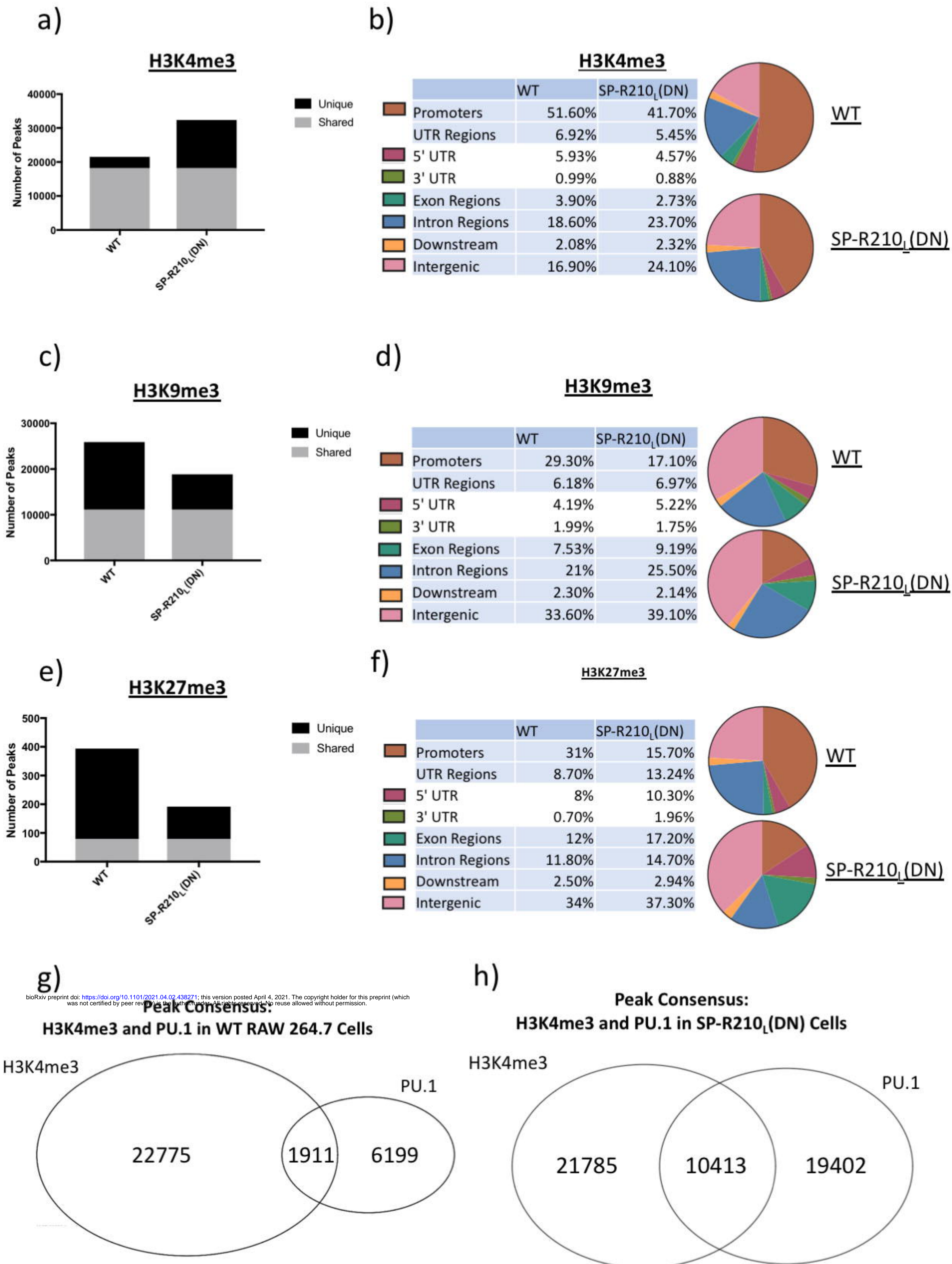
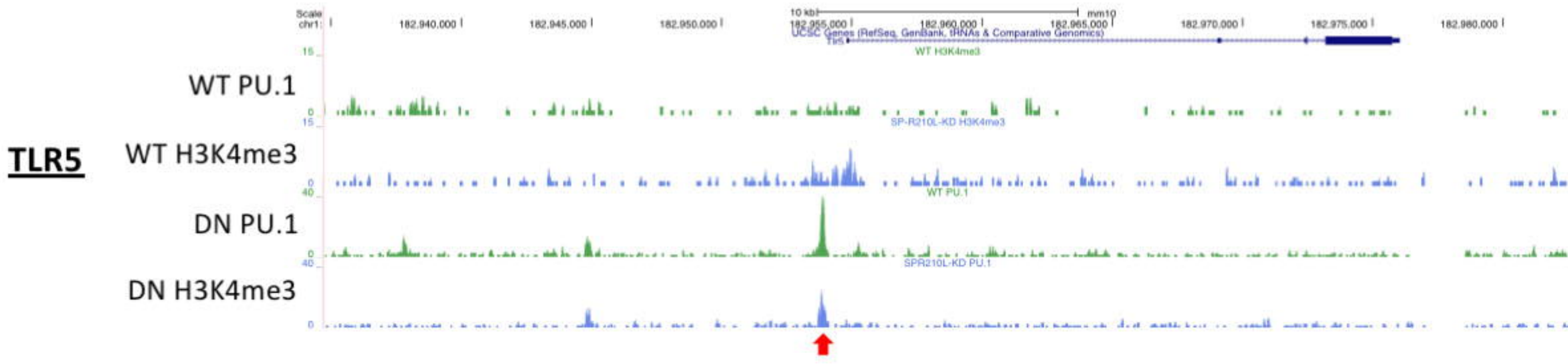
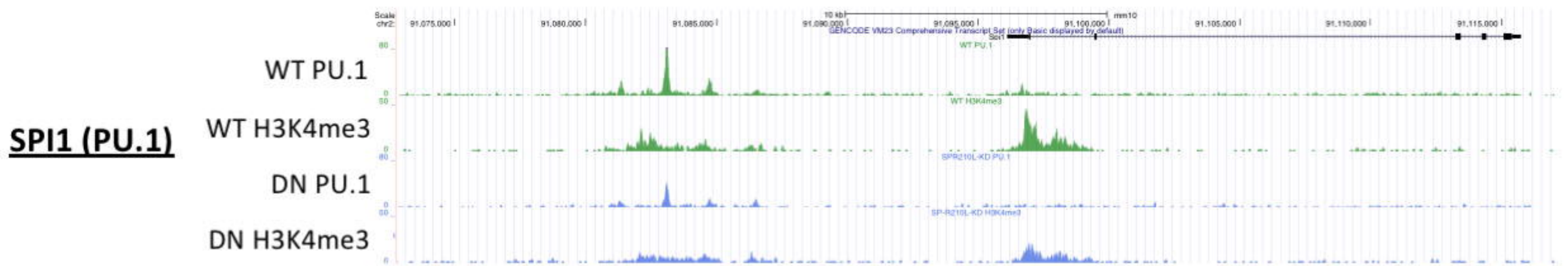


Figure 4

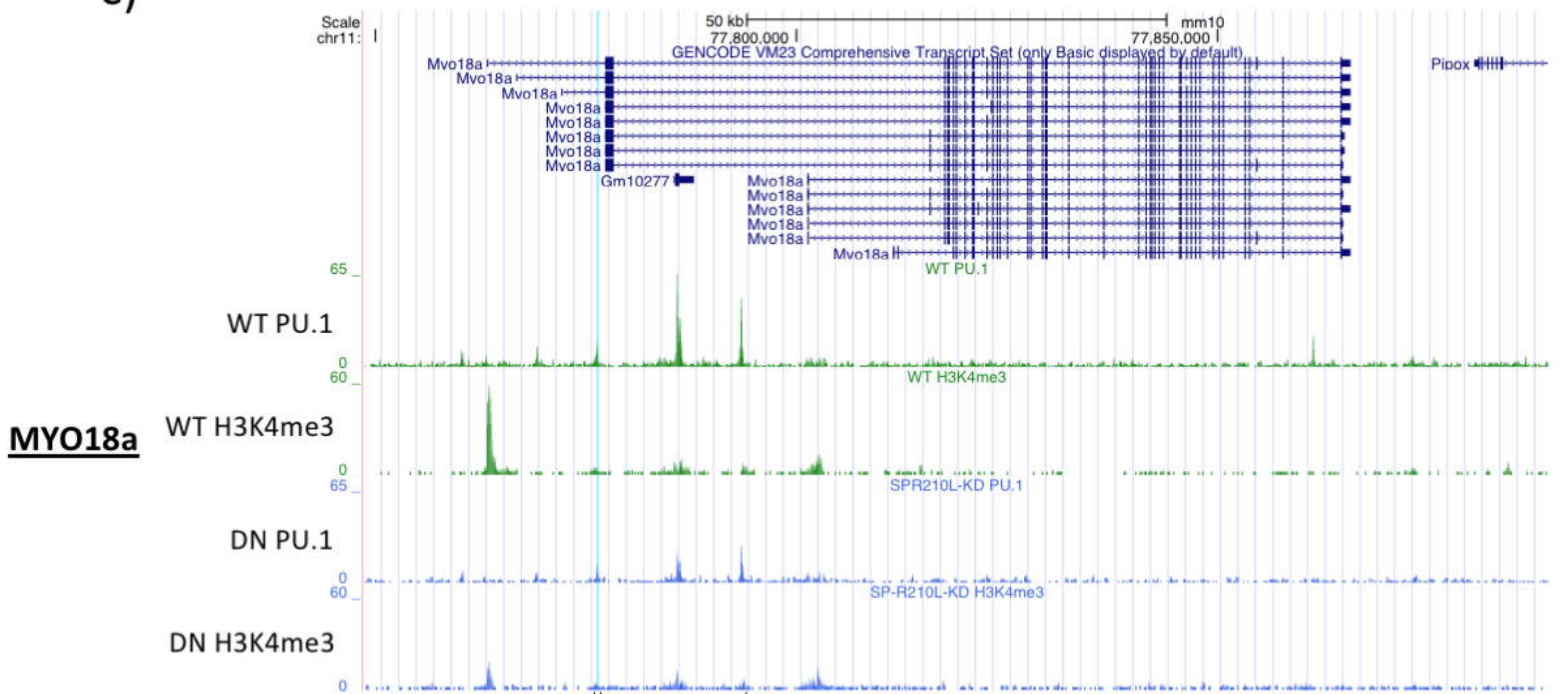
a)



b)



c)



bioRxiv preprint doi: <https://doi.org/10.1101/2021.04.02.438271>; this version posted April 4, 2021. The copyright holder for this preprint (which was not certified by peer review) is the author/funder. All rights reserved. No reuse allowed without permission.

TGGACTTCGTCTTC
77,776,326

AGGCGGAA CAGGAAGTGCAGTG
77,793,446

Figure 5

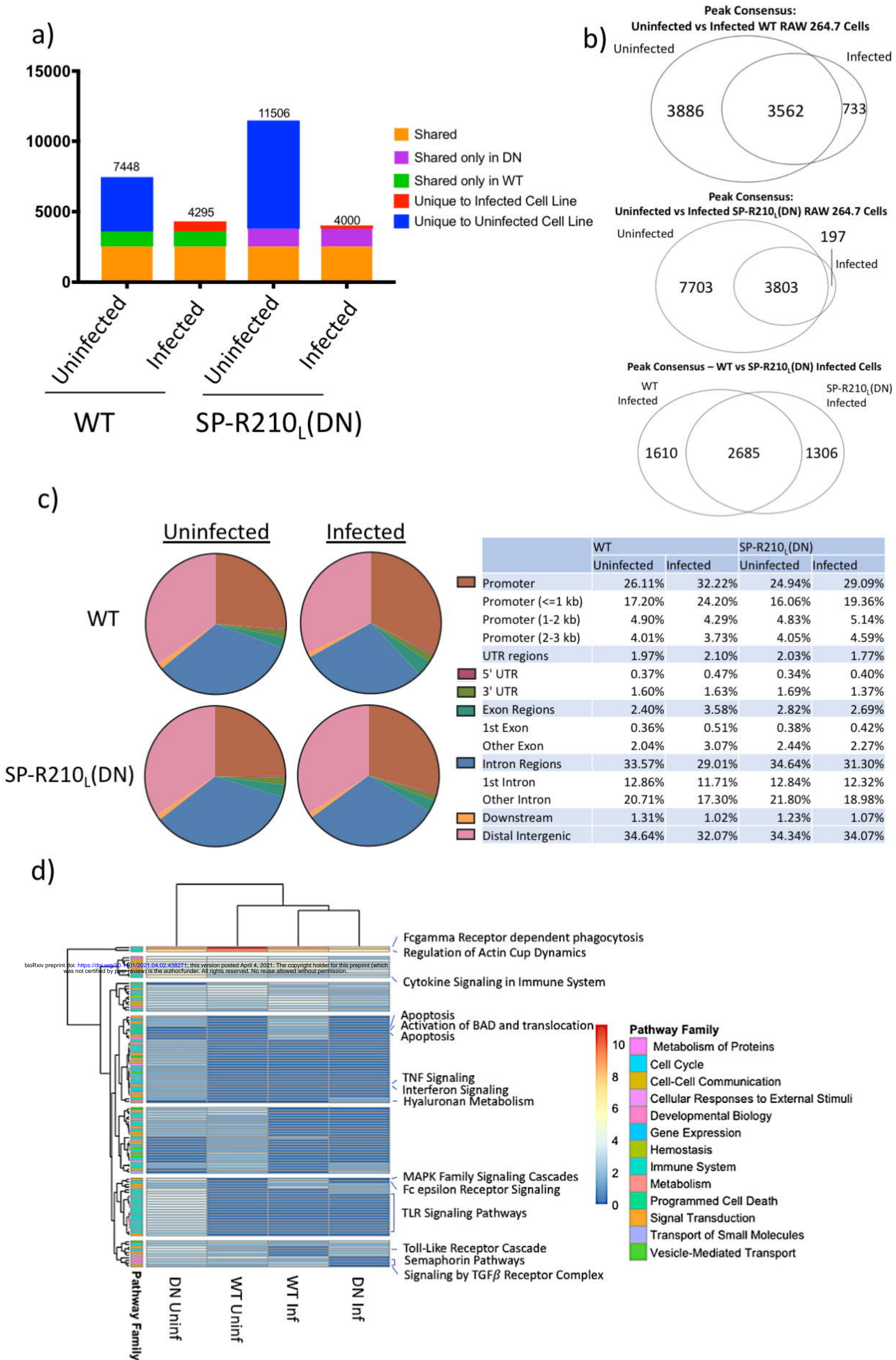


Figure 6

